

PLASMA JETS AND ERUPTIONS IN SOLAR CORONAL HOLES: A 3D FLUX EMERGENCE EXPERIMENT

F. MORENO-INSERTIS^{1,2}, K. GALSGAARD³

Draft version September 24, 2018

ABSTRACT

A three-dimensional numerical experiment of the launching of a hot and fast coronal jet followed by several violent eruptions is analyzed in detail. These events are initiated through the emergence of a magnetic flux rope from the solar interior into a coronal hole. We explore the evolution of the emerging magnetically-dominated plasma dome surmounted by a current sheet and the ensuing pattern of reconnection. A hot and fast coronal jet with inverted-Y shape is produced that shows properties comparable to those frequently observed with EUV and X-Ray detectors. We analyze its 3D shape, its inhomogeneous internal structure, and its rise and decay phases, lasting for some 15-20 min each. Particular attention is devoted to the field-line connectivities and the reconnection pattern. We also study the cool and high-density volume that appears encircling the emerged dome. The decay of the jet is followed by a violent phase with a total of five eruptions. The first of them seems to follow the general pattern of tether-cutting reconnection in a sheared arcade, although modified by the field topology created by the preceding reconnection evolution. The two following eruptions take place near and above the strong field-concentrations at the surface. They show a twisted, Ω -loop like rope expanding in height, with twist being turned into writhe, thus hinting at a kink instability (perhaps combined with a torus-instability) as the cause of the eruption. The succession of a main jet ejection and a number of violent eruptions that resemble mini-CME's and their physical properties suggest that this experiment may provide a model for the *blowout* jets recently proposed in the literature.

Subject headings: magnetic fields; magnetic reconnection; Sun: corona; Sun: flares; Sun: coronal mass ejections (CME's); Sun: X-rays

1. INTRODUCTION

X-ray and EUV plasma jets are a common occurrence in the solar corona, especially inside coronal holes and along their periphery. The first extended study of collimated plasma flows in X rays was achieved through the Yohkoh satellite in the 1990's (Shimojo et al. 1996; Shibata et al. 1992), albeit with limited spatial resolution (e.g., 2.5'' pixel size for Yohkoh-SXT). Images of the coronal jets in the EUV were obtained using the EIT instrument aboard the SOHO mission (Wang et al. 1998) and with the TRACE satellite (Alexander & Fletcher 1999). Substantial observational progress was obtained from 2006 onward with the soft X-ray telescope and the EUV spectrometer aboard the Hinode satellite (XRT and EIS, respectively, see Culhane et al. 2007a; Kano et al. 2008) and the EUVI and coronagraph imagers aboard STEREO. The Hinode mission allowed high space and time resolution observations of the jets in a large range of temperatures (e.g., for XRT, between 10^6 K and $3 \cdot 10^7$ K, with 1'' and 30 sec space and time resolution, respectively). They showed that the jets appear in large numbers in coronal holes, typically with an inverted-Y shape and with a set of hot magnetic loops at their base (Savcheva et al. 2007; Cirtain et al. 2007). The detailed statistics compiled by Savcheva et al. (2007), covering on the order of 100 jet events, indicates that their rate of oc-

currence is about 60 per day; their lifetime in soft X-rays has a broad distribution between about 5 and 30 minutes, peaking at 10 minutes; the jet velocity obtained through tracking of intensity changes in successive images ranges from 70 to about 500 km s^{-1} , peaking at about 160 km s^{-1} . The detection of much higher velocities (between 600 and 1000 km s^{-1} , Savcheva et al. 2007; 800 km s^{-1} , Cirtain et al. 2007) probably points to phase motions at the Alfvén speed rather than to actual mass transport velocities. Observed jet heights between 10 and 120 Mm and widths between 6 and 10 Mm were also reported by those authors.

Further insights were gained with the STEREO mission. Patsourakos et al. (2008) carried out stereoscopic observations of a polar coronal jet. By identifying the points on the jet front in EUV images, they found an impulsive acceleration to more than 300 km s^{-1} which roughly coincides with the appearance of an inverted-Y jet. The jet developed a helical structure suggestive of untwisting of magnetic field lines, perhaps following the development of a kink instability. Nisticò et al. (2009) studied jets that extended out to at least $1.7R_{\odot}$ and were observable in the EUV from both the A and B STEREO spacecraft. They found jets with an inverted-Y shape frequently associated with lower-lying coronal loops or bright points; they also find a minor subclass that have the characteristics of mini-CME events. A little less than half the events reported by those authors showed a helical structure. The lifetimes of these EUV jets ranged from about 5 to 70 min, with peaks between 20 to 30 min for the different wavelengths: in fact, the histograms depend on the wavelength, with shorter life-

¹ Instituto de Astrofísica de Canarias, Via Lactea, s/n, 38205 La Laguna (Tenerife), Spain

² Dept. of Astrophysics, Universidad de La Laguna, 38200 La Laguna (Tenerife), Spain

³ Niels Bohr Institute, University of Copenhagen, Juliane Mariesvej 30, 2100 Copenhagen

times for EUV lines formed at higher temperatures. This is in line with the even shorter lifetimes found for X-ray jets mentioned above. On the other hand, when using coronagraph images, the jets have much longer lifetimes, with the histogram peaking at around 70 to 80 min. More recently, Moore et al. (2010) have discussed a subclass of polar coronal hole X-ray jets (about one third of their sample), which they call *blowout jets*, which are counterparts of erupting-loop $H\alpha$ macrospicules. The members of the subclass are characterized by showing both a standard (or quiescent) jet and a more violent eruption at their base, possibly indicating that a flux rope is ejected, as in a mini-CME event (Innes et al. 2010). These observations are particularly interesting since, as shown in the current paper, the magnetic topology resulting from the emergence of magnetic flux into a coronal hole, subsequent reconnection and jet ejection is complicated enough for the system to strive to reduce its free energy via sudden eruptive events. Further instances of this sort of behavior have been discussed by Liu et al. (2011) and Madjarska (2011).

Concerning plasma properties in the jets, a Yokoh-based determination was provided by Shimojo & Shibata (2000). They found temperatures between 3 and 8 million K and densities between $7 \cdot 10^8$ and $4 \cdot 10^9 \text{ cm}^{-3}$. The recent work of Madjarska et al. (2012) finds lower temperatures, 2.5 million K, and densities around $10^{8.8} \text{ cm}^{-3}$ in the jets, and similar temperatures (but higher densities, $10^{9.5} \text{ cm}^{-3}$) at the base of the jets, although in a single case the temperature there reached at least $1.2 \cdot 10^7$ K. Further relevant references for the plasma properties of the jets are Culhane et al. (2007b); Madjarska & Wiegelmann (2009); Ding et al. (2010, 2011); Doscsek et al. (2010); Subramanian et al. (2010); Madjarska (2011). All in all, the observations support magnetic reconnection as the mechanism through which free magnetic energy is released and turned, via Joule heating, into thermal energy in the current sheet region, with temperatures reaching near 10^7 K, as well as into kinetic energy via the reconnection outflows, shock acceleration and subatomic particle acceleration.

The theoretical explanation for the jets has proceeded on the basis of detailed 2D and 3D numerical experiments using as starting point simple physical ideas about the triggering mechanism. The most explored theoretical idea is that the jets are produced when new magnetic flux emerges from the solar interior and collides with magnetic domains with simple (e.g., uniform field) configurations in the corona. This idea goes back to Heyvaerts et al. (1977), who proposed it as a mechanism to unleash flare eruptions. A related 2D numerical experiment was carried out by Forbes & Priest (1984). The first two-dimensional numerical MHD models of inverted-Y jet ejection following flux emergence from the solar interior were calculated by Yokoyama & Shibata (1995, 1996). Their models, which are strictly 2D (i.e., without velocity or magnetic field components in the direction of the ignorable coordinate), confirm that the interaction of a magnetic loop system emerging from the solar interior with an open, slanted field in the corona leads to the formation of a current sheet and ensuing reconnection at the interface between the two systems. The reconnection outflows, upon impinging onto the nearby

open field system, lead to a fast-mode shock which diverts part of the outgoing plasma upward along the open field lines, thus creating a jet at one end of the current sheet (see Fig. 9 in the paper by Yokoyama & Shibata 1996). The authors obtained a jet with velocity 0.6 times the background coronal Alfvén speed and temperature 1.6 times the background coronal temperature. At the other end of the current sheet, a set of closed coronal loops is created by the reconnection, which, therefore, also contain hot plasma. This experiment was a clear landmark. Yet, to alleviate the timestep restrictions of a realistic corona, the authors adopted unrealistic values for the density ($\approx 10^{12} \text{ cm}^{-3}$), temperature ($\approx 2.5 \cdot 10^5$ K) and Alfvén velocity ($\approx 84 \text{ km s}^{-1}$) of the background coronal model, obtaining jet temperatures and velocities far from the observed values. In recent years, Nishizuka et al. (2008) have repeated the Yokoyama & Shibata experiment, but now with $T = 10^6$ K and $n = 10^{10} \text{ cm}^{-3}$ in the corona. They obtain jet velocities and temperatures closer to the observations. The authors focus on the possible detection of Alfvén waves in the jet and on the quasi-simultaneous emission of neighboring hot and cold (10^4 K) plasma jets (see Sec. 8). They also discuss similarities with X-Ray, EUV and CaII observations.

Various other aspects of coronal jet emission following flux emergence have been explored the past years with 2D experiments. The reconnection in the 2D models may have an oscillatory character, as shown by Murray et al. (2009) through a 2.5D experiment (i.e., one that allows for non-zero velocity and magnetic field components along the ignorable coordinate): the emerged-field and hot-loop domains of the reconnection site change role as inflow and outflow regions for the reconnection in a damped oscillatory fashion following the corresponding increase and decrease of the gas pressure in them. McLaughlin et al. (2012) further investigated the dependence of the oscillations on model parameters.

The first numerical experiment in three dimensions of jet launching associated with magnetic flux emergence from the interior was reported in a Letter by Moreno-Insertis et al. (2008). Like in the earlier 2D experiments, their domain stretches from the top of the convection zone to the corona, but now the corona is endowed with realistic values of temperature ($1.1 \cdot 10^6$ K), density ($\approx 2 \cdot 10^8 \text{ cm}^{-3}$) and magnetic field (10 G) adequate for a coronal hole domain. The initial coronal field is uniform and inclined 25 deg from the vertical direction. The field emerging from below the photosphere is a twisted magnetic tube of the Ω -loop kind, as in the experiments by Archontis et al. (2004) or Galsgaard et al. (2007). The experiment showed that both the emerging domain and the hot reconnected coronal-loop region are dome-shaped, with the current sheet covering the top of the former. The jet itself had the canonical inverted-Y profile when seen in perspective from most orientations around the dome. High velocities (up to 200 km s^{-1}) and temperatures (slightly above 10^7 K) were measured in the jet, but it was not reported how volume-filling and permanent the high-T and high-velocity regions were in the jet evolution. A high-density region (10^{10} cm^{-3}) was found outside of the emerging dome roughly underneath the jet: it contains plasma formerly located in the emerged dome that has been dumped onto the open-field

domain as part of the reconnection process. The paper by Moreno-Insertis et al. (2008) also contained a comparison with Hinode/XRT and EIS observations of a hot coronal jet.

The aim of the current paper is to describe in detail a three-dimensional experiment of jet emission resulting from flux emergence from the solar interior that extends the work of Moreno-Insertis et al. (2008). Major differences to that paper are that our domain here is much larger, including a coronal volume of 68 Mm height, and that we pursue the experiment for an extended time, namely, about 80 minutes after initiation of the buoyancy instability leading to emergence into the atmosphere, which is well beyond the decay phase of the hot jet. We provide descriptions of the initial phases of the evolution, the current sheet, the jet, and the system of reconnected hot loops. The dense domain generated as a sub-product of the reconnection is also studied including Lagrange-tracing of the plasma elements. Further, a series of violent eruptions starting at different positions of the emerged flux rope could be detected: we count five eruptions in total, all taking place after the jet was already in the advanced decay phase. This links our experiment with a number of flux emergence simulations of the past ten years which focused on flux-rope eruptions (Manchester et al. 2004; Archontis & Török 2008; Archontis & Hood 2008, 2012; MacTaggart & Hood 2009), and also with the experiments of Török & Kliem (2003, 2005); Pariat et al. (2009, 2010) and Aulanier et al. (2010), who obtained eruptions following kink- or torus-instability patterns not associated with magnetic flux emergence from the interior. The first of the flux emergence references given above (Manchester et al. 2004) describes how the emerged domain is subjected to shear across the main polarity inversion line (PIL) turning into a sheared arcade. A vertical current sheet is formed and reconnection ensues, following a pattern not completely unlike the classical mechanism of Carmichael (1964), Sturrock (1966), Hirayama (1974), and Kopp & Pneuman (1976) for the launching of a flare: a flux rope is violently ejected upward containing the reconnected top part of the original arcade; simultaneously, a sort of *post-flare* magnetic arcade is created at the bottom end of the sheet. In our experiment, we obtain a first eruption centered between the opposite-polarity roots of the emerged domain that follows this general pattern even if importantly modified through the different coronal field configuration prior to the flux emergence. The subsequent eruptions, however, take place on the sides of the emerged active regions and may contain a combination of the kink and torus instabilities in them.

The layout of the present paper is as follows. In Section 2 we provide details of the numerical model. Section 3 discusses the initial evolution and the structure after emergence. In section 4 the main phase of the jet activity is presented, including details of the current sheet, the reconnection and the jet itself, as well as of the closed loop system resulting from the reconnection. Section 5 describes the formation of a cold density region encircling the emerged domain. Section 6 describes the series of repeated eruptions that take place after the decay of the jet, including details of the magnetic connectivity changes that result from them. Section 7 looks into the evolution of global quantities, like the axial magnetic flux

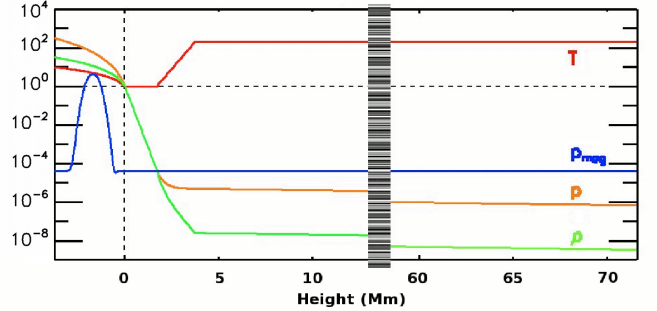


Figure 1. Stratification in the initial model. Shown are the temperature (red), gas pressure (orange) and density (green) as a function of height z at $t = 0$ far from the magnetic tube, normalized to their photospheric value. The blue line is the magnetic pressure distribution along a vertical line passing through the center of the initial tube in the same units as the gas pressure. For clarity, the central sections of the corona have been omitted.

or the interior-to-corona magnetic connectivity. Finally, section 8 contains a summary and discussion.

2. MODEL AND EQUATIONS

We model the emergence of a twisted magnetic flux rope from underneath the solar surface into an open-field domain in the corona. Three basic structural elements at the initial time are, therefore: (a) the background stratification; (b) the ambient coronal magnetic field; and (c) the subphotospheric magnetic tube. The initial background model is similar to that used in our previous papers on 3D flux emergence models (see Archontis et al. 2004), but with a very extended corona. In Fig. 1 we present the dependence of temperature (T_{st} , red), density (ρ_{st} , green) and pressure (p_{st} , orange) with height (z) at time $t = 0$, all normalized to their photospheric ($z = 0$) values. The domain consists of four regions in hydrostatic equilibrium representing, from bottom to top, the uppermost 3.74 Mm of the convection zone (assumed adiabatically stratified), the low atmosphere (a domain between $z = 0$ and $z = 1.70$ Mm initially with uniform temperature, T_{phot}), a transition region between $z = 1.70$ and $z = 3.74$ Mm, and above it the corona, that extends for 67.9 Mm and has $T = 200 T_{phot}$. The units of temperature, density and pressure for the calculation are taken to be the photospheric values, namely: $T_{phot} = 5.6 \cdot 10^3$ K, $\rho_{phot} = 3 \cdot 10^{-7}$ g cm $^{-3}$ and $p_{phot} = 1.4 \cdot 10^5$ erg cm $^{-3}$. This leads to the following units of velocity: $c_{phot} = \sqrt{p_{phot}/\rho_{phot}} = 6.8$ km sec $^{-1}$; length: $H_p = p_{phot}/(\rho_{phot} g_{\odot}) = 170$ km; and time: $\tau = 25$ sec. The coronal values for temperature and particle density that follow from those choices are: $T_{cor} = 1.1 \cdot 10^6$ K and n_{part} between $5.9 \cdot 10^8$ cm $^{-3}$ and $4.3 \cdot 10^9$ cm $^{-3}$, respectively, which are reasonable values for a coronal hole atmosphere (Wilhelm 2006; Harvey & Recely 2002). Like in the previous papers, an elementary ideal gas with uniform specific heats is used here for simplicity.

To mimic a coronal hole medium, the corona must be endowed with an open magnetic field. To that end, we add in the whole box a uniform ambient magnetic field of 10 G intensity contained in the $x - z$ plane and inclined an angle $\alpha = 25$ deg to the vertical, $\mathbf{B} = B_c (-\sin \alpha \mathbf{e}_x + \cos \alpha \mathbf{e}_z)$, with \mathbf{e}_i indicating the basic unit vectors and B_c the field strength. This is of course a potential field, so the original hydrostatic equilibrium is preserved. The associated plasma β is small in the corona (between 0.12

and 0.02); on the other hand, this field is dynamically irrelevant in the photosphere and below, where $\beta > 3 \cdot 10^4$.

The initial setup is completed by embedding a horizontal, twisted magnetic flux rope oriented along the y -axis below the photosphere at $z = -1.7$ Mm. Like in the earlier experiments, the prescription for this field follows Fan (2001): using cylindrical coordinates (r, θ, y) around the tube's axis, the field components are given by:

$$B_r = 0; \quad B_\theta = q r B_y; \quad B_y = B_0 \exp(-r^2/R^2); \quad (1)$$

with q a constant twist parameter. This yields a single value of the pitch, $2\pi/q$, for all field lines. Here we are using $B_0 = 3.8$ kG, $R = 0.4$ Mm, and $q = 2.4$ Mm $^{-1}$, leading to a total axial magnetic flux of $2.2 \cdot 10^{19}$ Mx, which is in the range of the ephemeral active regions. The choice of sign for q is such that it leads to opposition between the direction of the B_θ component of the tube and the ambient coronal field described above. The magnetic pressure distribution for the total (tube + ambient) field along a vertical line that intersects the tube axis can be seen as a blue solid line in Fig. 1. The gas pressure is then modified from $p = p_{st}$ to $p = p_{st} + p'$ in such a way that the sum of Lorentz and gas pressure forces, $\mathbf{F}_{Lor} - \nabla p$, has the same value as before introducing the magnetic tube; hence, the hydrostatic equilibrium is preserved. This choice is always possible since the Lorentz force for the given field is curl-free. Finally, the horizontal magnetic tube is made buoyant by increasing the entropy of its plasma elements for a limited distance in y around $y = 0$ but without modifying the pressure. The resulting density perturbation, $\rho' = \rho - \rho_{st}$, is of the form $\rho'/\rho_{st} = (p'/p_{st}) \exp(-y^2/\Lambda^2) \leq 0$. We choose $\Lambda = 3.4$ Mm.

The experiment is solved in a Cartesian domain of size 48.3 Mm x 33.9 Mm x 75.4 Mm in (x, y, z) , respectively. This domain is substantially taller than in all our previous 3D flux emergence experiments, and includes, in particular, 71.6 Mm above the photosphere. This is done so that we can capture a substantial distance along the jet and to separate completely the top boundary domain from any region of interest in the box. Concerning the boundary conditions, the domain is taken to be periodic in the horizontal directions. The boundaries in the vertical direction are impenetrable and with zero horizontal velocity. This basic setup would reflect any propagating perturbation hitting the top and bottom boundaries, which would be undesirable, especially since a jet is meant to propagate upward in the box. Hence, a non-reflecting damping layer is implemented near those boundaries: we use an algorithm of the Newton-cooling type that brings the density, internal energy and momenta back toward their $t = 0$ values on a timescale that increases with distance from the boundary.

The evolution of the experiment is followed in time by solving the non-ideal MHD equations (as given in the paper by Archontis et al. 2004) using the Copenhagen Stagger Code which contains hyperdiffusive ohmic and viscous terms self-consistently included in the induction, momentum and energy equations (Nordlund & Galsgaard 1997). The numerical box used has 448 x 320 x 512 points in the (x, y, z) directions, respectively. The grid is uniform in the horizontal directions with about 100 km resolution. In the vertical direction, we use a

stretched grid to better resolve the low atmosphere and the reconnection site that produces the jet. We have a vertical resolution of 30 km at the photospheric level and of 100 km at a height of 10 Mm above the photosphere.

3. INITIAL PHASES AND STRUCTURE AFTER EMERGENCE

The initial stages of the evolution share many common features with previous papers based on similar initial conditions (like, e.g., Archontis et al. 2004, 2005; Galsgaard et al. 2007; Moreno-Insertis et al. 2008; Murray et al. 2009). The central part of the tube, which, following the prescriptions explained in Sec. 2, has a small density deficit compared with its surroundings, $|\rho'/\rho_{st}| = O(0.04)$, rises toward the photosphere leading to an Ω -loop shape for the tube. The rise to the surface takes some 10 minutes. The temporary slowing down in those levels and the development of a secondary buoyancy instability there take a further 10 min, approximately, and are as described or analyzed by different authors (e.g., for the secondary buoyancy instability, Magara 2001 in 2D and Archontis et al. 2004, Moreno-Insertis 2006 and Murray et al. 2006 in 3D). This buoyancy instability leads to the runaway rise of magnetized plasma. By time $t = 25$ min, for instance, one can see a roundish hill of strongly magnetized material pushing into the corona with its summit located about 3 Mm above the photosphere (as in Fig. 2, bottom panel, but less expanded than in that more advanced time) and showing an abrupt drop of magnetic pressure between the emerged material and the ambient corona. By time $t = 27$ min, i.e., still quite early in the evolution, the drop has turned into a smooth transition and the emerged system, while still magnetically dominated [$\beta \sim O(10^{-2})$], enters a slower rising phase, characterized by a quasi-equilibrium between the outward-pointing magnetic pressure gradient force and the inward-pointing magnetic tension force. This approximately force-free phase is possible since the Alfvén crossing time is short, below 1 min, well below the evolutionary time scale dictated by the instability development. During this phase the magnetic field strength in the emerged dome decreases with height following quite accurately an exponential law, with scaleheight $H_B \approx 1.5$ Mm at $t = 30$ min and $H_B \approx 2.3$ Mm at $t = 40$ min. This is reminiscent of the self-similar expansion evolution described by Shibata et al. (1989) for the 2D development of a buoyancy instability in a magnetic layer.

In these early stages the emerged plasma is very dense compared to the initial unperturbed values at the same height: ρ values corresponding to heights between 1 and 2 Mm in the initial atmosphere appear now on a much larger range of heights (e.g., up to 6 Mm by time $t = 30$ min). Yet, gravity is small compared with the components of the Lorentz force in this region: the H_B values quoted above yield ratios $v_A^2/H_B \gg g_\odot$, so that the plasma can only fall along the field lines. The velocity pattern in the emerged plasma in this phase is then comparatively simple: still propelled by the buoyancy instability, the rising mountain continues its advance into the atmosphere with an almost force-free magnetic field configuration. The plasma in it slides down along the field lines thereby reaching velocities on the order of the free-fall value (e.g., about 40 km s $^{-1}$ for an element falling under gravity for a distance of about 5 Mm). When seen

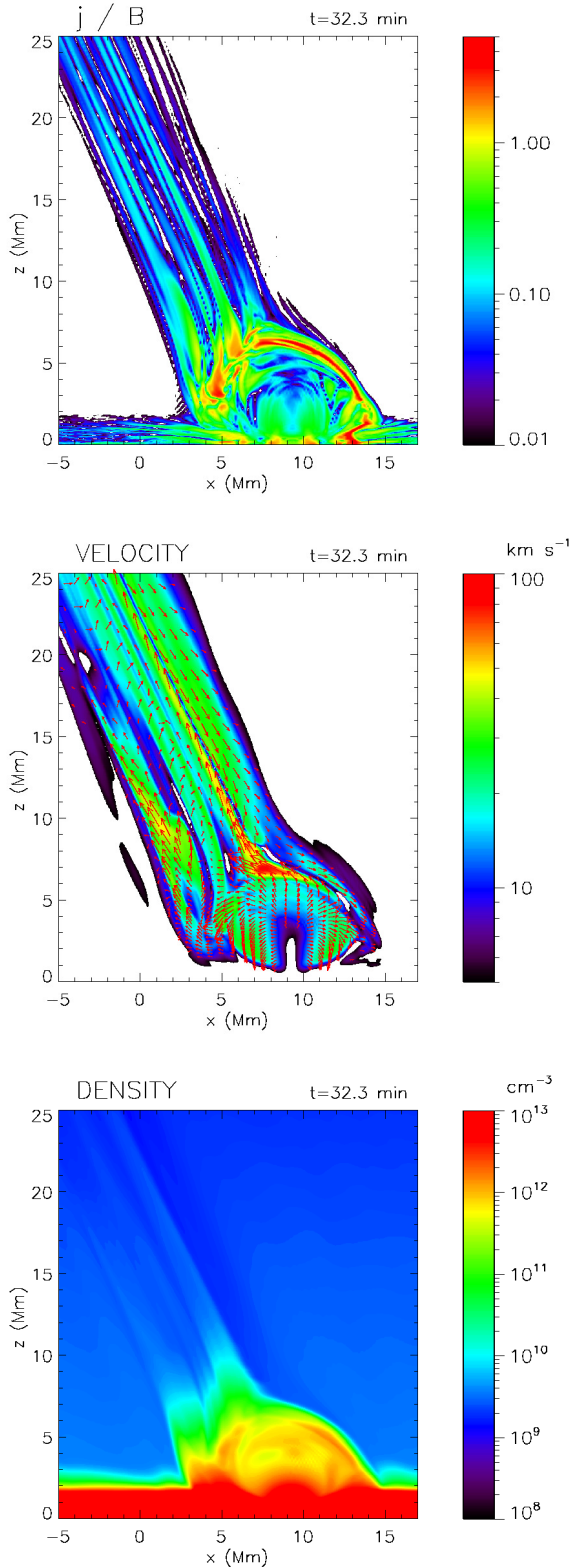


Figure 2. 2D vertical cut across the box at $y = 0$, i.e., perpendicular to the initial axis of the tube. Shown are color maps of $|j|/|B|$ (top), $|v|$ (center) and ρ (bottom) at an early time of the jet evolution, $t = 32.3$ min. Variable values below the minimum of the colorbar are drawn in white. The current sheet at the periphery of the emerged dome is visible as a thin red stripe (top panel). The maximum velocity (82 km sec^{-1}) is reached in the reconnection region.

in a two-dimensional cut, the velocity field pattern has a characteristic fountain-like shape (still visible at a later time through the arrows in the dome-shaped domain of Fig. 2, central panel).

Soon after entering the atmosphere, a prominent current sheet is formed at the periphery of the emerging plasma mountain (as visible in the form of a red stripe around the dome in Fig. 2, top panel, for $t = 32$ min). This current sheet directly results from the conflict of orientations of the azimuthal magnetic field component of the rising tube with the ambient coronal field. In 3D one can see that the sheet covers, as a blanket, all that side of the rising mountain. Reconnection sets in across the current sheet from the early stages of the emergence and is already well under way at the time shown in Fig. 2 ($t = 32$ min). The central panel of the figure shows a color map of $|v|$, with, superimposed as red arrows, the projection of the velocity vector on the $x - z$ plane. The plasma is being ejected from the current sheet toward the ambient corona on the left of the figure. The inflow into the sheet both from the corona and from below, i.e., from the emerged dome, is also apparent. Feeding the current sheet from the corona, in particular, creates a downflow from high up along the coronal field lines adjacent to the reconnection site. At this early stage, however, the reconnection-related velocities are not large: several tens of km sec^{-1} in the coronal downflow, and up to 100 km sec^{-1} in the reconnection outflow. It is also visible in the figure that there is an ejection of plasma (hence, of reconnected field lines) further out to the left (e.g., for $x < 3 \text{ Mm}$). Those field lines carry the dense material from the emerged mountain with themselves, producing a cool, dense region next to the emerged dome: the green, spike-like area to the left of the reconnection site in the central panel [e.g. $(x, z) \sim (2, 8) \text{ Mm}$] might be taken as a sort of cool jet with velocities of several 10s of km sec^{-1} . Yet, in fact, when seen in 3D, one realizes that the cool region encircles the emerged dome and has no obvious jet shape. Details are given in Sec. 5. The bottom panel of Fig. 2 will be discussed in the next section.

4. THE MAIN PHASE OF JET ACTIVITY

Following the standard picture, the reconnection taking place across the thin current sheet lets magnetic field and plasma from the emerged system join the field and plasma coming down from the corona and ejects them toward either end of the sheet. The situation is comparatively easy to describe by using a vertical cut of the system in the $x-z$ direction, as in Figs. 2 and 3. The reconnected field lines ejected toward the left-hand side of the figure become open field lines rooted in the photosphere. The reconnection outflow in that direction leads to the creation of an upward moving jet along the field lines, which is studied in detail in subsection 4.1 below. It also leads to flows pointing toward the photosphere along the left flank of the emerged dome; their discussion is deferred to Sec. 5. The reconnection outflows that point toward the right-hand side of the current sheet in the figure lead to the formation of a system of coronal loops (i.e., with both footpoints rooted in the photosphere) which are studied in Sec. 4.2. Finally, the *jet engine*, the reconnection in the current sheet, is studied in Sec. 4.3.

4.1. Time evolution of the jet

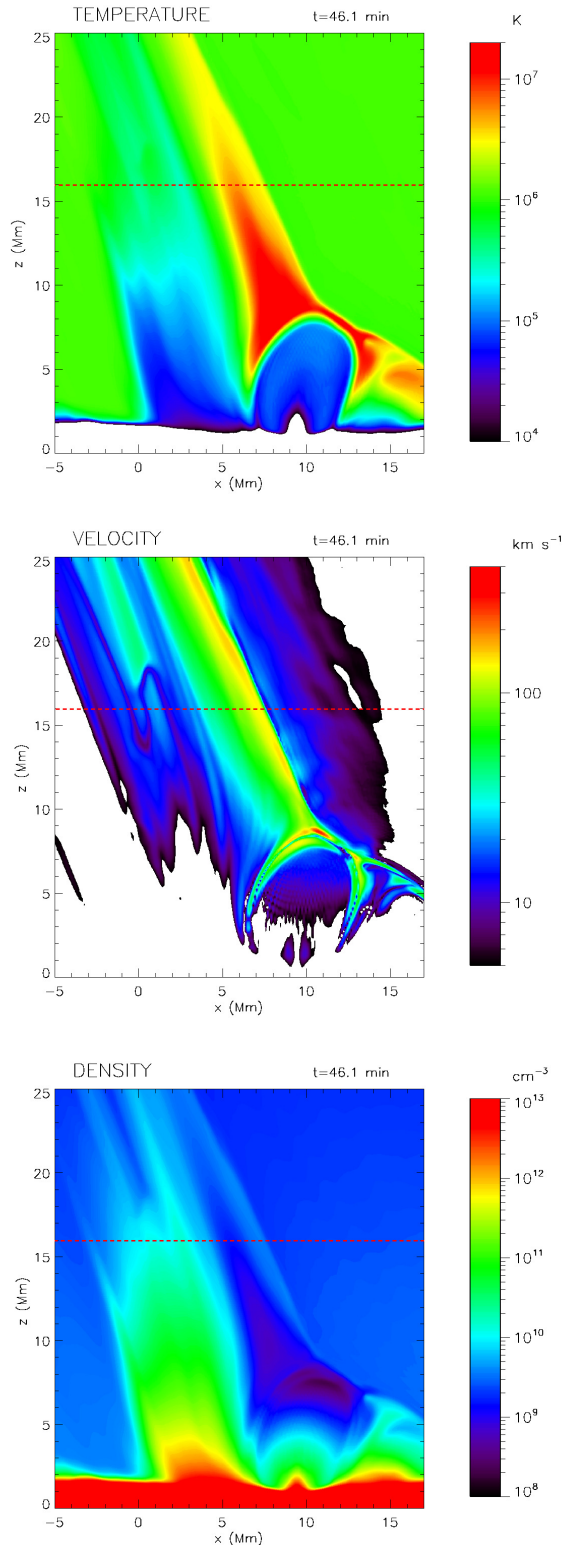


Figure 3. 2D maps for the same vertical plane as for Fig. 2 toward the peak of the jet activity ($t = 46$ min). The panels here correspond to temperature (top), $|\mathbf{v}|$ (center), and density ρ (bottom). Variable values below the minimum of the colorbar are drawn in white. The maximum values of temperature ($2.2 \cdot 10^7$ K) and velocity (290 km sec^{-1}) in the domain shown are reached in the reconnection region. The red dashed line indicates the height used for Fig. 5

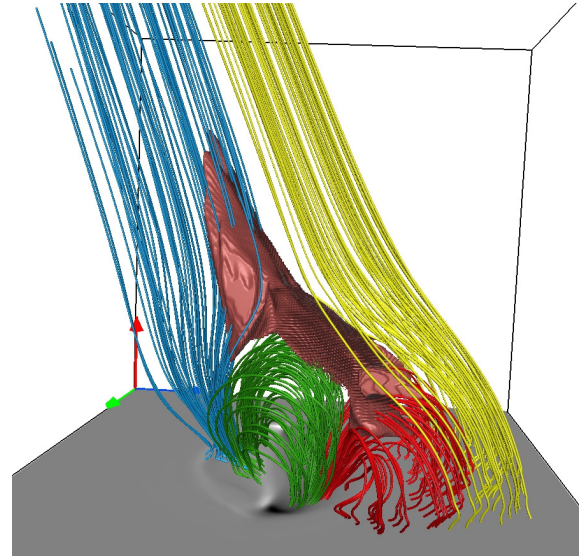


Figure 4. 3D view of the jet (visualized through a temperature isosurface) and field lines of the different flux systems

In the early phase, the material in the emerged system is very dense (Fig. 2, bottom panel), with ρ being above the density of the ambient coronal plasma at the same height by one or two orders of magnitude. Consequently, the reconnection outflows and the ensuing jet strands do not have high temperature. However, as a consequence of the continued drainage of plasma along the field lines explained in the previous section, the material in the emerged region becomes increasingly rarefied. Hence, at the peak of the reconnection process (Fig. 3), we find that an important part of the plasma flowing into the current sheet from below has a low density (Fig. 3, bottom panel), even down to an order of magnitude below the ambient coronal values. The ohmic heating taking place in the current sheet, therefore, can raise their temperature to high levels (Fig. 3, top panel), up to $O(10^7 \text{ K})$ in the neighborhood of the sheet. The result, seen in the 2D projection of Fig. 3, is a triangular region (actually, of inverted-Y shape) with low ρ and high T values in the lowermost $\sim 10 \text{ Mm}$ of the jet. The time evolution of the temperature in that vertical plane can be studied through an accompanying movie. A 3D view is provided in Fig. 4: the figure includes a magnetogram at the photosphere showing the strong negative surface polarity at the front; there is also a temperature isosurface (brown) at $T = 7 \cdot 10^6 \text{ K}$, that contains in its interior the reconnection site and delineates the beginning of the jet and the top of the hot loops formed after reconnection. The four field line systems visible in the figure are described in Sec. 4.3.

If we now turn to the velocities ($|\mathbf{v}|$, Fig. 3, central panel), the maximum values are not reached in the bulk of the hot and rarefied material, but, actually, in a thin layer covering the jet as a blanket. This can be seen through the horizontal cuts shown in Fig. 5. The top row shows 2D maps of $|\mathbf{v}|$ and T on a horizontal plane cutting the jet at height 16 Mm above the photosphere (some 8 Mm above the reconnection region, as indicated by a horizontal dashed line in Fig. 3) at the time of peak jet activity, $t \sim 45$ min. We clearly see that the jet is actually a curved sheet-like structure, with plasma moving

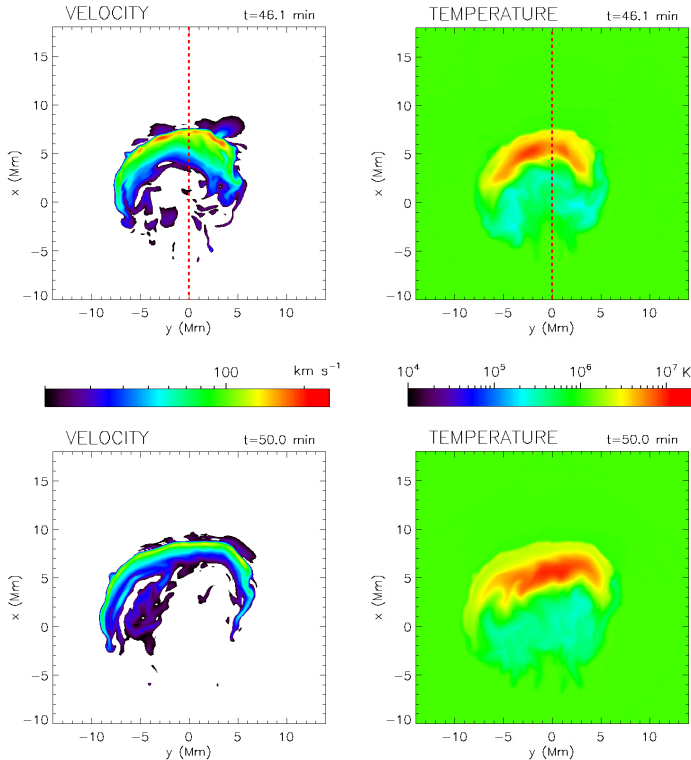


Figure 5. Color maps of velocity (left) and temperature (right) on a horizontal cut taken at a height of 16 Mm above the photosphere cutting across the jet. Top row: $t = 46.1$ min (simultaneous with Fig. 3). Bottom row: $t = 50.0$ min. A number of high-velocity strands are visible in the top-left panel. The jet is seen as a bent surface containing different layers: an external high-velocity sheet, and a more internal hot layer. The red dashed line in the top panels indicates the location of the cut in Fig. 3

at velocities around 150 km s^{-1} but with a number of individual high-velocity streams embedded in it (top left panel). The maximum temperatures (top right panel), about 5 million K, are, again, not uniformly distributed in the sheet, and, in fact, are not reached at the site of maximum velocity. This situation becomes more marked along the decay phase of the jet ($t \sim 50$ min, bottom panels): the high-velocity part of the jet is now (bottom left) a very thin sheet located on the side of the non-reconnected coronal plasma. On the inner side of that sheet, a high-temperature domain (a little below 10^7 K) can still be found, co-spatial with the low density domain discussed above (bottom right). The shift between the high velocity jet and the high temperature region seen in the figure is caused by the decrease in time of the temperature of the jet: the high temperature region corresponds to older and hotter ejected material whose motion upward along the jet has been slowed down. A further feature can be seen in the temperature maps: there is a cool patch [light-blue, $O(10^5 \text{ K})$] underlying the hottest blob: this cool patch is not part of the jet but, rather, corresponds to the topmost reaches of the cool dense domain described in Sec. 5. The time evolution of the maximum velocity and temperature in the horizontal plane at $z = 16$ Mm is presented in Fig. 6. During the main phase of the jet ($t < 65$ min, i.e., left of the vertical dashed line), the maximum velocity is about 250 km s^{-1} and the maximum temperature close to 10^7

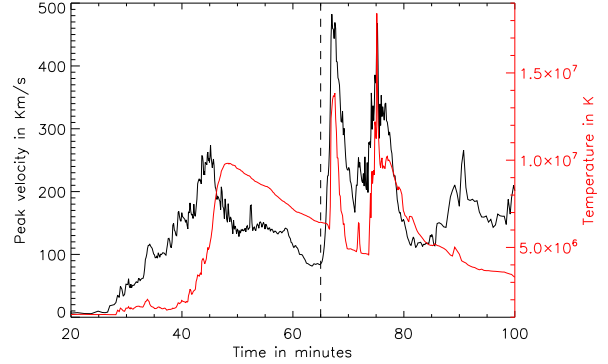


Figure 6. Time evolution of the maximum velocity (black) and temperature (red) in a horizontal cross section of the jet at $z = 16$ Mm. To the left of the vertical dashed line one sees the evolution during the main phase of the jet. To the right, the violent eruption phase described in Sec. 6

K. The rise and decay sections of the velocity curve in that phase have a similar duration, some 15 – 20 min in either case; the temperature shows a rapid rising phase (5 min) followed by a more extended decline. After $t > 65$ min, a series of violent eruptions take place, as described in Sec. 6.

4.2. The reconnected coronal loops

Going back to Figs. 3 and 4, we now turn our attention to the reconnected field lines that are being expelled from the current sheet toward the right of the figure. Given the magnetic topology, these are closed magnetic loops (in red in Fig. 4), linking the photospheric domain of the emerged field with the surface roots of the preexisting coronal field: Fig. 4 shows that they partially encircle the emerged dome on one of its sides, constituting an almost semicircular arcade. They come out of the reconnection layer with a high level of shear, but turn to configurations nearer to force-free as time proceeds. The temperature at the top of the loops follows a pattern as seen for the jet in Sec. 4.1: first the temperatures are cool, but then they rise to a peak of order 10^7 K, which is reached broadly coinciding with the peak of the red curve in Fig. 6. Given their high temperatures, we will often refer to these loops in the following as *the hot coronal loops*.

The reconnected loop region grows in size as time proceeds at the expense of the emerged domain, since new reconnected loops are formed from the latter that pile up on top of the previous ones. This can be seen by comparing the top panel of Fig. 3 with the corresponding panel of the earlier time (shown in Fig. 2). In fact, we will see in a later section (Fig. 11) that the emerged region is being exhausted and turns in later phases into a vertically elongated wedge. The growth of the reconnected loop domain is also related to another phenomenon which is amenable to observational comparison: the actual jet drifts toward the positive x -direction (i.e., to the right of the 2D plots) as time advances. This is a consequence of the reconnection process: the corresponding decrease of the tension of the coronal field allows the current sheet to move so as to maintain a sufficient stress in the system and continuously feed the jet with new material. Monitoring the sideways motion of the jet on the $y = 0$ plane at z between 10 and 15 Mm we obtain velocities of 7 to 8 km sec^{-1} around $t = 30$ min, which then gradually

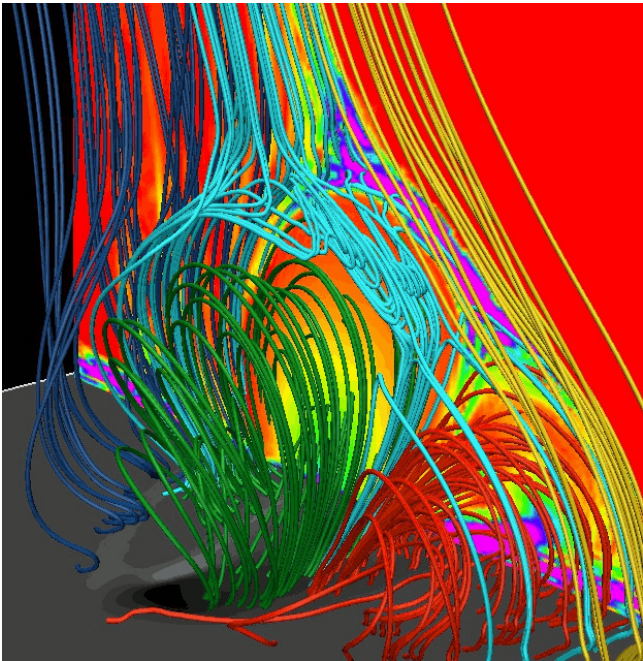


Figure 7. Illustration to the field line topology in the current sheet explained in Sec. 4.3

decrease, becoming very low, 2 km sec^{-1} , by $t = 65 \text{ min}$, i.e., at the time of initiation of the first eruption.

4.3. The current sheet and the reconnection region

The reconnection taking place in the current sheet is of a fully 3D nature. Going back to the 3D view provided in Fig. 4, we can discern four different sets of magnetic field line systems: (1) at the top-right, the ambient coronal field lines (yellow) being fed to the reconnection site joining (2) the emerged magnetic loops (green) which link the opposite polarities at the surface. On the left, (3) the blue lines are reconnected field lines that maintain their open-field nature: Even though they appear similar in shape to the original coronal hole field lines, the reconnection process and ensuing episodes are causing strong dynamical and thermodynamical perturbations in the plasma attached to them. Finally, (4), at the bottom right, a set of closed magnetic loops (red) as described in Sec. 4.2 that link the photospheric domain of emergence with the external photospheric field. The magnetic topology shown in Fig. 4 looks deceptively simple. On the one hand, there appear plasmoids within the current sheet, which, given their 3D nature, are in fact solenoids wrapping around the general hill-shape of the emerged material (see Archontis et al. 2006). This is shown in Fig. 7. The vertical panel contains a map of $|j|/|\mathbf{B}|$: the purple-colored concentrated current sheet is apparent. The light-blue field lines were traced so that they pass preferentially near the null points. The other field line sets in the figure are as described in Fig. 4. The light-blue lines clearly show a collection of 3D plasmoids, with a solenoidal appearance, embedded in the collapsed current sheet. In fact, additionally to using visualization techniques, we could detect the presence of a number of null points within the current sheet using a null-point finder program (Haynes & Parnell 2007); they turn out to be contained in a small range of the axial (y) coordinate, and slowly move in the direction of the neg-

ative surface polarity as the jet develops. The presence of plasmoids indicates that multiple episodes of tearing instability have occurred in the sheet.

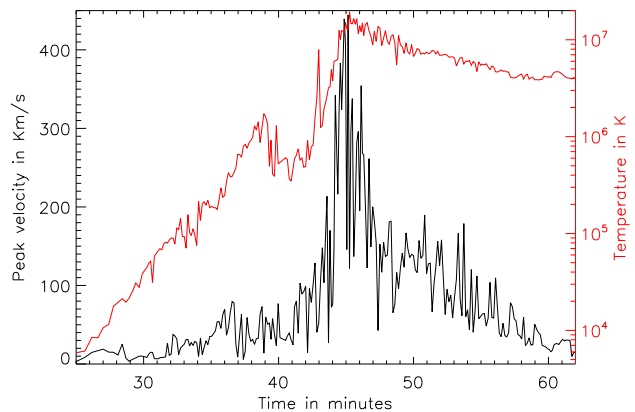


Figure 8. Time evolution of velocity (black) and temperature (red) in the current sheet, tracked by determining the location of minimum $|\mathbf{B}|$. When comparing with Fig. 6, note the linear temperature scale in that figure.

The time evolution of the current sheet can be measured through various quantities. As a proxy for the location of the reconnection site we have chosen the point in the current sheet, $\mathbf{r}_{rp} \equiv (x_{rp}, y_{rp}, z_{rp})$, where $|\mathbf{B}|$ reaches its minimum, B_{min} . This procedure does not lead to an accurate position determination, but is good enough to provide approximate numbers for the temperatures and velocities near the reconnection site, probably in the neighborhood of a null point. In Fig. 8, the temperature (red) and velocity (black) measured at \mathbf{r}_{rp} are plotted for the duration of the main phase of the jet. We can see that the rise and decay of the temperature and velocity in the current sheet correlate well with those in the jet discussed in Sec. 4.1 (see Fig. 6). The peak velocity, in particular, is higher than the corresponding peak value in Fig. 6. By tracking in time the position of B_{min} , we see that it rises by $\sim 5 \text{ Mm}$ before remaining at $z = 7 \text{ Mm}$ in the decay phase; horizontally, it also slides by $\sim 7 \text{ Mm}$ into the $y > 0$ half space (where the negative photospheric polarity is located). Instead, it does not move much in x (i.e., the abscissas of Figs. 2 or 3): it looks as though the region with the null points is *sliding around the flanks of the emerged mountain*. This impression is confirmed by following the actual motion of the null points in time and will be further discussed in Sec. 6.

5. THE COLD PERIPHERY: THE DENSE WALL

In previous sections we mentioned the presence of a relatively cold and dense volume surrounding the emerged magnetic loops as a wall. A visualization of this structure is provided in Fig. 9. The panel on the left contains a density map on a horizontal cut at $z = 4 \text{ Mm}$ and $t = 47 \text{ min}$, i.e., near the peak phase of the jet activity. The map clearly shows the very dense surroundings of the emerged-loop region, like a ring or wall, with densities generally between 10^{11} and 10^{12} cm^{-3} , peaking at the back of the structure, i.e., below the jet. In the figure, arrows corresponding to the horizontal projection of the magnetic field have been added. The location of

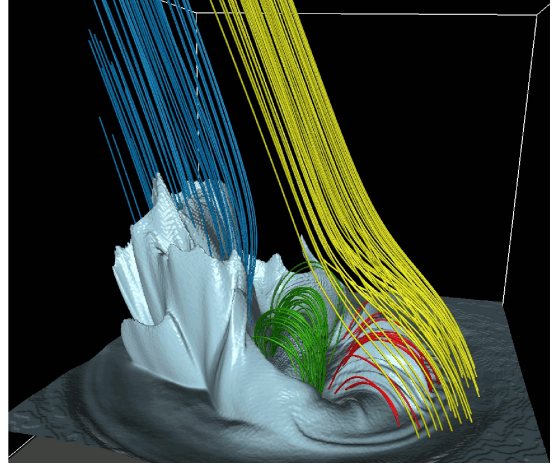
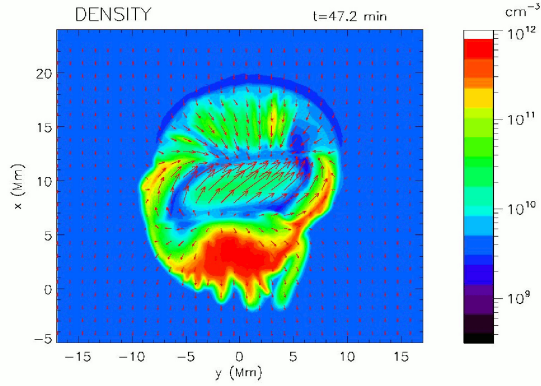


Figure 9. Illustration of the high-density wall. Left: density map on a horizontal plane 4 Mm above the photosphere – the arrows show the horizontal projection of the magnetic field vector. Right: 3D visualization of the dense domain using a density isosurface at $\rho = 4 \cdot 10^{10} \text{ cm}^{-3}$ and field lines from the different magnetic connectivities illustrated in Fig. 4

this ring or wall with respect to the emerged loop system can be seen in the 3D image in the right panel of the figure: the image contains an isosurface of the number density for $n = 4 \cdot 10^{10} \text{ cm}^{-3}$ (bright to dark grey) and includes selected field lines of the different magnetic systems (same color code as for Fig. 4). The isosurface has a crater-shape with ragged peaks around a hole, and is continued sideways by a roughly horizontal domain until the boundaries of the box. In the central hole we see the (green) magnetic arcade of the emerged domain. The reconnected coronal loops (red) are almost covered by this isosurface; the highest density peaks are located in the reconnected region below the jet (blue field lines). Both reconnected systems have inherited the high densities of the emerged material. At this time, however, the emerged region is already very rarefied (Sec. 4.1, Fig. 3, bottom panel), and this is the reason for the central hole of the density isosurface. The maximum elevation of the isosurface is several Mm. The dense wall is clearly a 3D phenomenon: it appears all around the emerged domain, although its shape depends on the actual location relative to the emerged flux system. The dense domain has transition region temperatures, between a few times 10^4 and a few times 10^5 K , well below coronal values.

To disclose the origin and nature of this dense wall, we have used Lagrange tracing for the plasma elements. For the tracing, we interpolate \mathbf{v} between snapshots, which had been taken with high time cadence (between 8 and 16 sec in this phase). Figure 10 shows the position of the tracer particles at different times in the experiment. For the figure, we selected an initial box with tracers distributed uniformly between approximately $z = -0.3 \text{ Mm}$ and $z = 20 \text{ Mm}$, and covering horizontally a large fraction of the emerging region. The top of the box is located therefore some 10 Mm above the top of the emerged dome in the main jet phase. Each particle is given a color according to its instantaneous density (colorbar on the right). We note that green ($n \sim 6 \cdot 10^{10}$ to $2 \cdot 10^{12} \text{ cm}^{-3}$, say) corresponds to heights 1.9 to 2.8 Mm in the initial atmosphere, whereas dark blue ($n \sim 3 \cdot 10^8 - 10^9 \text{ cm}^{-3}$) corresponds to coronal densities. We had two different Lagrange-tracing runs (top and bottom rows in the figure, respectively), with initial boxes of the same size and position and with the same initial tracer distribution, but

with different starting times. The sequence in the top row was started at time $t = 20.8 \text{ min}$ (left panel), i.e., when the top of the rising flux tube was still at the photosphere. The tracers in the initial Lagrange box with green and blue colors thus correspond to plasma that was in the atmosphere before the flux emergence takes place, attached to inclined coronal field lines. The times for the other three panels in that row are, from left to right, 35.4, 43.8 and 62.5 min, respectively.

The panels in the top row show how the mass elements in the atmosphere change position following the arrival of the tube. At the time of the second and third panels, the magnetic tube has already fully emerged (its top is in fact located at about $z = 8 \text{ Mm}$). Most of the tracer particles of the pre-emergence material have been moved to the left where they constitute part of the dense region visible in Fig. 9 (right panel, e.g., the volume delineated by the grey isosurface). The way in which that happens is: those particles are attached to coronal field lines that somewhere along their length are pulled down into the approaching reconnection region. This of course does not imply that the Lagrange particles themselves go through the reconnection domain: it is the field lines they are attached to that must go through the (spatially small) diffusion region where the change of magnetic connectivity takes place. Those that reach the region on the left at early stages end up in the dense-volume visible on the left hand side. The two rightmost panels show how the particles that go over to the reconnected side in the more advanced stages are likely to be launched along the jet with high speeds (keeping a density on the order of their initial coronal value – see the deep-purple set of particles in the upper half of the box). The rightmost panel also shows how at that late time the pre-emergence material has been completely vacated from the position of the emerging dome. The velocities found in the dense domain on the left are not large ($\lesssim 50 \text{ km sec}^{-1}$).

The lower row of panels illustrates further aspects of the plasma evolution. This sequence was started at time 45.8 min of the simulation, i.e., near the third panel from the left in the top row. A large part of the initial Lagrange box for this series contains emerged material. We see in the second and third panels (green colored particle domains) how a fraction of these particles go over

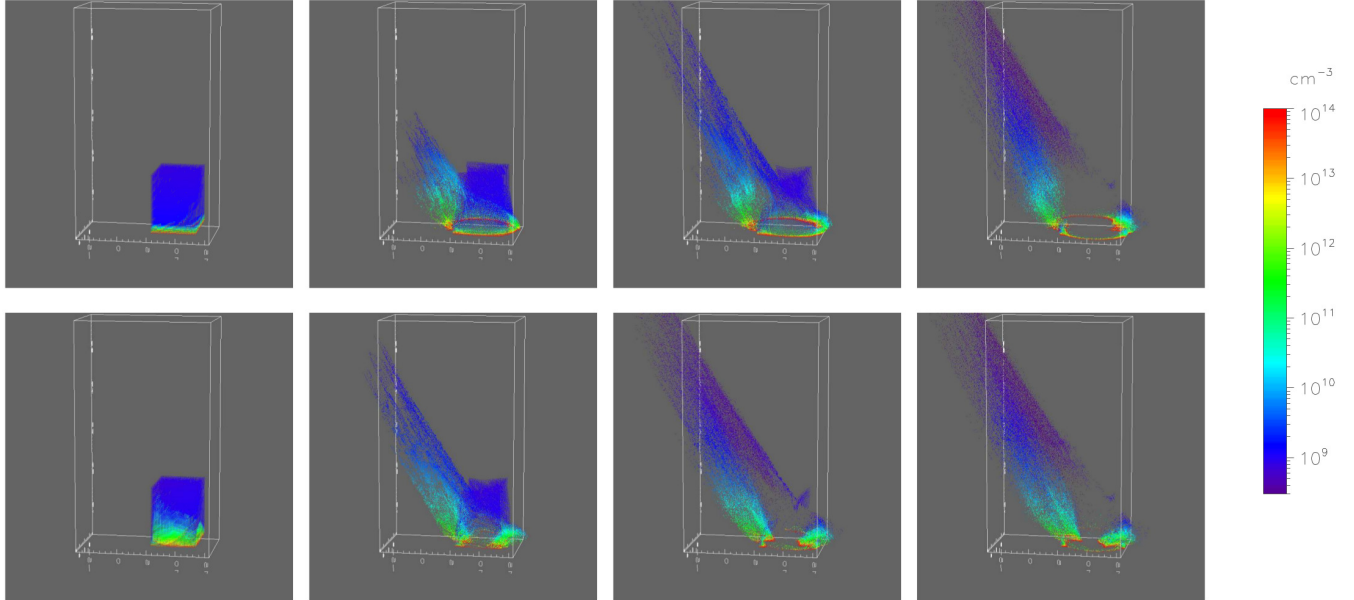


Figure 10. The frames show the time evolution of the Lagrange tracing particles. Each row corresponds to a different tracing sequence, with the leftmost frame being the respective initial condition. The times for the top row frames are $t = 20.8, 35.4, 43.8$ and 62.5 min; those for the bottom row are $t = 45.8, 51.7, 57.5$ and 62.9 min. The color coding for the particles corresponds to the local plasma number density. See also the accompanying movies.

to the dense wall domain. Those particles are attached to field lines that are undergoing reconnection. As explained for the top row, however, the particles themselves need not go through or near the reconnection point: their field lines take the particles with them over to the reconnected domain, without necessarily being part of the high-velocity reconnection outflows or jets. Analyzing the images in this series, one could say that the emerging dome is progressively peeling itself off of its external layers, passing its dense external layers little by little onto the reconnected systems (open field, closed-loop systems). Again here, the velocities for the green-colored particles in the third rightmost panels in this row are not large ($\lesssim 50 \text{ km sec}^{-1}$). On the other hand, another fraction of the particles really go near the reconnection site, get accelerated and end up being part of the jet, hurled upward with the high speeds mentioned in Sec. 4. As a final item, a fraction of the particles in either time sequence are attached to field lines that end up in the reconnected loop system on the right of the figure.

The formation of a dense circular wall constituted in part by debris from the emerged material seems to be a rather natural feature in the process described in this paper. One wonders if any part of the cool and dense material discussed so far could really be seen as constituting a cool $\text{H}\alpha$ surge or CaII jet, as proposed in the literature (see, e.g., Yokoyama & Shibata 1996; Miyagoshi & Yokoyama 2003; Nishizuka et al. 2008). This is discussed in Sec. 8.

6. ADVANCED PHASES

The rather smooth evolution described in the previous sections ends abruptly at $t \sim 65$ min. There follows a more dramatic phase, with several violent eruptions occurring in different parts of the emerged structure: to the end of the experiment ($t = 100$ min), we have located

five such eruptions, and there is no reason to assume the series would stop at that time. In this section we discuss these events and their relation to eruptions found in previous flux emergence experiments.

6.1. First eruption: a variation of the sheared arcade instability

The field line configuration right before the start of the first eruption is illustrated in Fig.11: in the top panel, a magnetogram, i.e., the grey-scale map of $B_z(z=0)$, shows the bipolar region with its two strong opposite polarities which is clearly developing a sigmoidal shape of positive helicity. Two sets of field lines have been drawn in that panel: the one in red corresponds to the inner core of the emerged flux rope, which is not far above the photosphere and very nearly delineates the polarity inversion line (PIL). The green field lines identify the magnetic system that is still remaining in the emerged plasma domain. To better illustrate this, the central panel additionally shows a map of the electric current (precisely: of $|\mathbf{j}|/|\mathbf{B}|$) on the vertical plane at $y=0$. We see in the image that the green field lines of the previous panel go through the cross section of what remains of the emerged dome: the continued peeling off of plasma and field lines from the latter has turned it into a thin wedge with a narrow base. We also recognize a strong and thin current sheet (purple) toward the upper-right corner, topping up the wedge. To the right of the wedge in the figure, the hot-coronal loop region (which was a relatively small feature in the early stages, see Figs. 3 and 4) has become quite large: we have drawn a bunch of field lines (in light brown), which show the general geometry of the field there. We see that a thin, almost vertical current sheet has built up at the base of the wedge; to investigate its nature, in the bottom panel we draw in blue a further set of field lines (and remove the

green and brown ones for clarity): the new set has been selected so that they pass through the wedge cross section at intermediate heights; we see that those lines are part of a highly sheared magnetic arcade. We also see the reason for the current concentration: the arcade has footpoints of opposite polarity near each other, ready to undergo reconnection.

The first eruption takes place in the time frame between, approximately, $t = 64$ minutes and $t = 70$ minutes. The opposite-polarity feet of the field lines in the sheared arcade (blue field lines in Fig. 11, bottom panel) get close enough to each other for fast magnetic reconnection to start. The first stages of this process strongly resemble the *tether cutting* reconnection scheme extensively discussed in the literature (see Mikic et al. 1988; Sturrock 1989; Moore & Roumeliotis 1992; Moore et al. 2010), in particular in relation with the emergence of flux ropes through the photosphere (Manchester et al. 2004; Archontis & Török 2008; Archontis & Hood 2008, 2012): the reconnection creates two sets of field lines at either end of the thin quasi-vertical current sheet created at the feet of the sheared arcade; the one at the top is a twisted magnetic rope that is hurled upward whereas the one below is a simple arcade that progressively turns into a quasi-potential configuration, as described below. The reconnection process, however, soon becomes much more complicated than in the standard flare situation. The reconnection between opposite polarities at the feet of the original sheared arcade is asymmetric: the arcade field lines on one of the sides of the current sheet become fully reconnected while there is still remnant arcade flux on the other side. As a result, field lines from the hot loop system (like some of those in light brown in the central panel of Fig. 11) start to be reconnected with those remnant field lines from the arcade (light-blue field lines in Fig. 11). In the final stages of the eruption, field from the open magnetic system (not shown) at the far end of the wedge in Fig. 11 get in contact with field lines from the hot loop system (light brown) and reconnect across the current sheet. The resulting connectivity scheme can be discerned through Fig. 12. In the top panel we are showing bunches of field lines illustrating five of the different connectivity patterns just discussed: the green field lines are the heirs of the green field line system in Fig. 11 and are ejected toward the beginning of the reconnection process; the yellow and dark blue field line sets correspond to the new connectivities created in the advanced stages of the eruption, namely sheared-arcade connected with hot coronal loops (yellow) and open field lines connected with hot coronal loops (dark blue). The other two sets are best discussed using the bottom panel of the figure: in it we are including a color map of $|\mathbf{j}|/|\mathbf{B}|$ on the vertical plane at $y = 0$ that clearly shows (a) the thin current sheet below the erupted material (in purple), (b) the current sheet at the interface between the erupted material and the ambient coronal field, and (c) the complication of the erupted region, in which plasma attached to the field lines of the different stages of the reconnection is moving with high speed and expanding sideways. In this panel we are also showing a small arch system near the photosphere (in light-blue color, but not to be confused with the light-blue system in Fig. 11): this is indeed the result of reconnection at the bottom end of the thin current sheet; we note that it has a much lower shear than

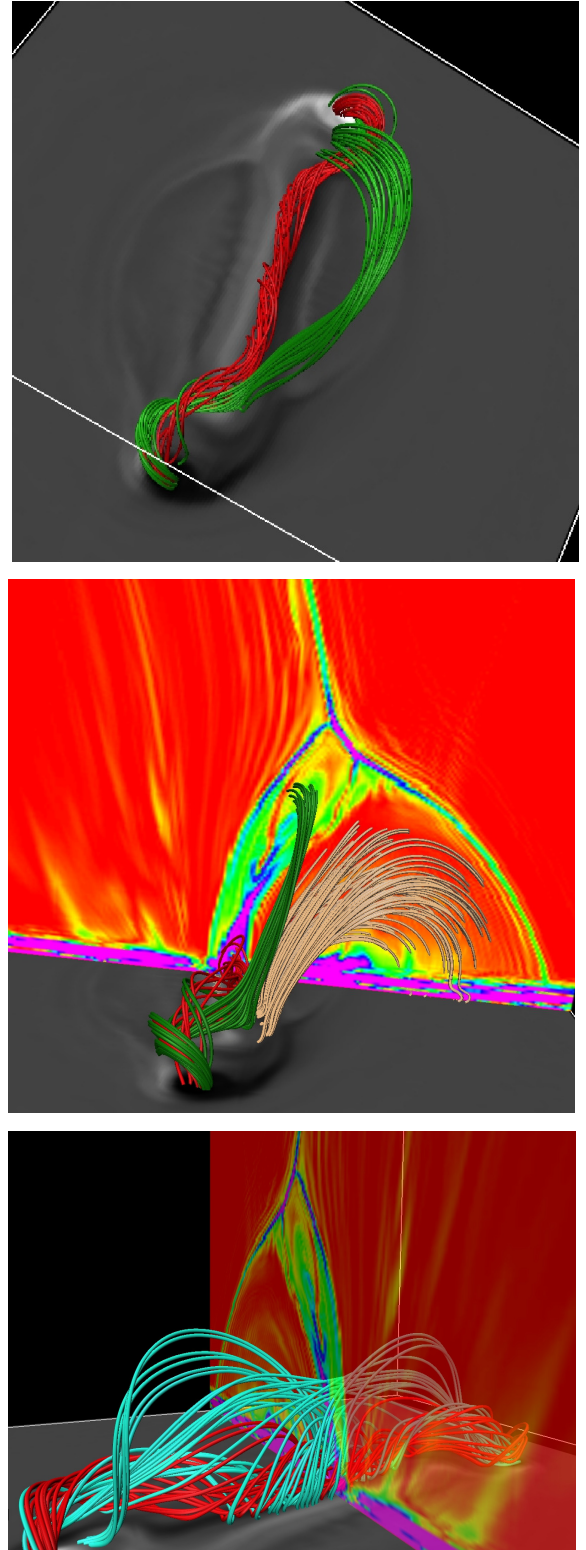


Figure 11. Illustration of the field-line and electric current configuration right before the start of the first eruption ($t = 64.5$ min). The grey-scale map in all panels is a *magnetogram*, meaning the distribution of B_z at the level $z = 0$. The vertical color map (central and bottom panels) corresponds to $|\mathbf{j}|/|\mathbf{B}|$ in arbitrary units, and extends between red (lowest value) and purple (highest value). The different field line sets illustrate characteristic connectivity patterns, as explained in the text. Note that the vertical plane is seen from opposite sides in the middle and bottom panels.

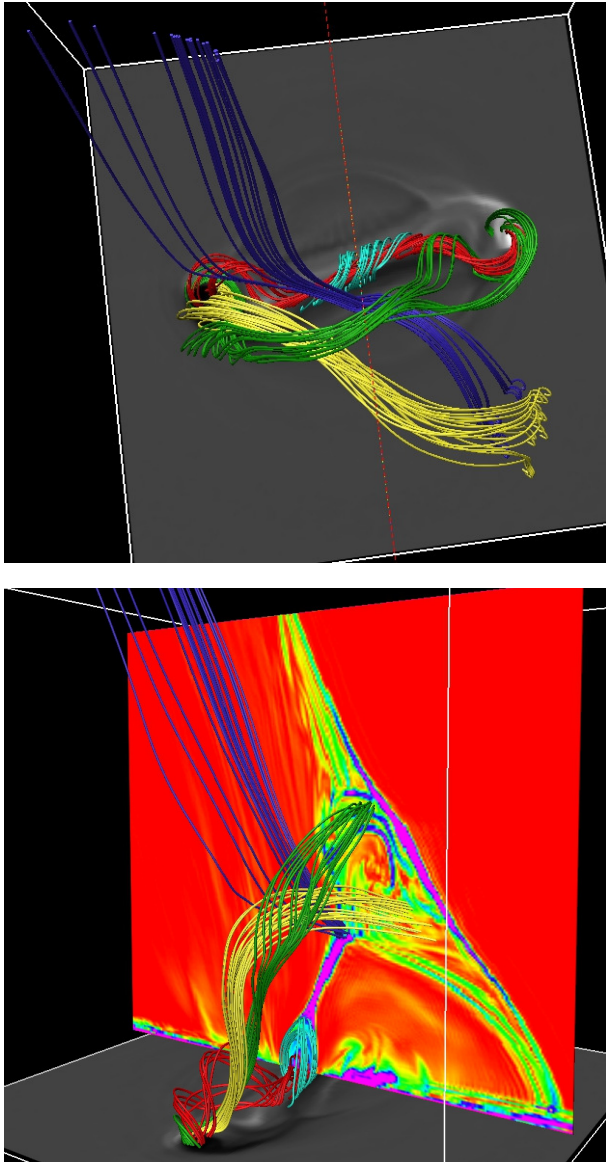


Figure 12. Field line connectivity and current distribution as the first eruption is unfolding $t \sim 65.9$ min. Upper panel: top view showing the magnetogram at the $z = 0$ level and five sets of field lines representative of major connectivity patterns at that time. Lower panel: map of $|j|/|B|$ on the central vertical plane ($y = 0$), showing the current sheet located underneath the flux rope that contains what remains of the emerged material.

the original arcade. The red field line system, finally, is the original core of the emerged flux rope, essentially the same system as shown in red in Fig. 11.

The erupting material in the successive stages is hurled onto the overlying open field with high velocity, around 600 km s^{-1} at its core. The ambient coronal magnetic field outside of the jet is strong enough to withstand the impact; the eruption, therefore, is channeled along the field lines where the original jet was propagating and disturbs their neighborhood. The eruption will be seen not only to perturb a large part of the emerged domain (as explained below), but, also, to propagate as a sort of short-lived, impulsive jet with a complex structure roughly in the same direction of the original jet. The differences in field line orientation between the erupted

material and the open field create the thin current sheet that delimits the perturbed domain toward the top-right corner in the lower panel of Fig. 12, through which reconnection occurs. The strong perturbation caused by this eruption is communicated along the field lines and ejected upward reaching the top levels of the numerical box. The maximum temperature and velocity in the horizontal plane $z = 16 \text{ Mm}$ plotted in see Fig. 6 show a pronounced peak of about $1.4 \cdot 10^7 \text{ K}$ and about 500 km sec^{-1} , respectively, during this eruption. The kinetic energy in the volume where the eruption takes place goes through a marked peak of $8 \cdot 10^{26} \text{ erg}$.

6.2. The off-center eruptions

Four further eruptions occur in the remaining ≈ 30 minutes of the experiment: they all start and mainly take place in the *flanks* of the active region, i.e., in the general volume above the strong polarities at the photosphere. Their evolution also has a number of further features that distinguish them from the first eruption, and also among each other. In the following we describe the main traits of the first two of these off-center eruptions: covering all of them goes beyond the scope of the present paper.

The eruption discussed in the previous subsection (Sec. 6.1) starts in the low coronal heights midway between the two opposite polarities at the photosphere (i.e., around $y = 0$). Yet, the large perturbation quickly gets communicated to the flanks, i.e., to the levels above the strong photospheric polarities. This occurs through a variety of phenomena: referring to Figs. 11 and 12, first, not only does the erupting flux rope (set of green field lines in either figure) rise, but, also, its roots reach regions nearer the two opposite photospheric polarities; second, the number of hybrid, reconnected field lines of the kind colored in yellow in Fig. 12 increases as time goes on, thus communicating the perturbation to the regions nearer the negative polarity visible in that figure (i.e., toward the $y > 0$ half-space). However, there is a region roughly above the PIL close to the strong negative photospheric polarity that is not very much affected by the first eruption: this coincides with the strongly curved, hook-like shaped region of the PIL near the negative polarity at the surface apparent in Figs. 11 (top panel) and 12. The unperturbed region can also be seen in Fig. 13, top panel, where a vertical map of $|j|/|B|$ in the neighborhood of the strong negative polarity is shown corresponding to $t = 66$ min (same time as for Fig. 12). Three separate closed regions (labeled regions 1 through 3) can be discerned adjacent to each other in the plane, two with a wedge shape and a roundish one on the right: the central one (region 2) is the result of the strong perturbation caused by the first eruption; the upward-pointing wedge-shaped region to the left (region 1) contains magnetic field of the initial emerged tube: two field line sets have been drawn: the bottom one (in red) is quite twisted and considerably inclined; it nearly follows the curved, hook-like shape of the PIL near the negative surface polarity; the field-line set in green is less twisted but, like the red one, links to the regions near the PIL on the side of the vertical plane of the figure. These field line sets appear not to have changed topology nor their general shape as a result of the eruption at the center: we will see presently (Sec. 6.2.2) that a violent eruption takes place shortly after the time of the figure starting from field lines like

the red ones in that panel. The roundish area on the right (region 3), finally, corresponds to the hot coronal-loop region which, again, is not greatly affected by the eruption. In the following we describe two events that take place in this end (the $y > 0$ end) of the emerged domain: namely, the reconnection event occurring near the prominent null point situated in that neighborhood (Sec. 6.2.1), and the development of the eruption just mentioned.

6.2.1. The null point above the negative photospheric polarity

The complicated null-point and plasmoid structure of the reconnection site described in Sec. 4.3 (Fig. 7) becomes increasingly simple as it slides sideways along the y -direction in the decay phase of the jet toward the negative-polarity end of the active region; at time $t = 50 - 55$ min, in fact, the magnetic skeleton here contains a single null point with real eigenvalues. At this time the fan surface is locally near horizontal; on the one side it represents the canopy of the hot loop system and, on the other, it divides the emerging flux from the open flux region. The electric current in the fan surface near the null increases its intensity in the phase up to the second eruption; doing this the current sheet expands in width, and the distance between the *roots* of the two spine axes move apart, attaching to the edges of the current sheet (See Pontin et al. 2007 for a detailed description of this kind of null collapse).

The location of the null and the structure of its skeleton at the time of the first eruption ($t = 66$ min) is illustrated through the light green and red sets of field lines in the central panel of Fig. 13. A plasmoid (delineated by the green field lines as labeled in the panel) is seen to occupy the site of the current sheet, indicating that the latter has undergone a tearing instability. This behavior of null point evolution is seen in various dedicated numerical experiments of asymmetric single 3D nulls that are being stressed (Galsgaard & Pontin 2011). The reconnection process that we can deduce from the numerical data is of the type known as spine-fan reconnection (Priest & Pontin 2009), where flux is being transported through the fan surface and spine axis from one topological domain to another. In fact, as illustrated in Fig. 13 (central panel), the reconnection involves the flux rope of the previous eruption (red field lines in the figure): as it continues to reach higher levels, it starts interacting with the stressed null point and the field line connectivity changes, allowing these field lines to connect the positive surface flux concentration with the open field region, whereas, in turn, the left-hand side footpoint becomes connected to field lines near the downward-pointing spine.

The comparatively simple topological structure just described is deeply modified by the second eruption, which causes the creation of a cluster of null points in the current sheet.

6.2.2. The second eruption

As already indicated, in the region of the upward-pointing wedge visible on the top panel of Fig. 13, the low-lying arched and twisted flux rope is starting to move upward with increasing speed, leading to the second eruption. The situation at an intermediate stage of the process can be followed through the bottom panel

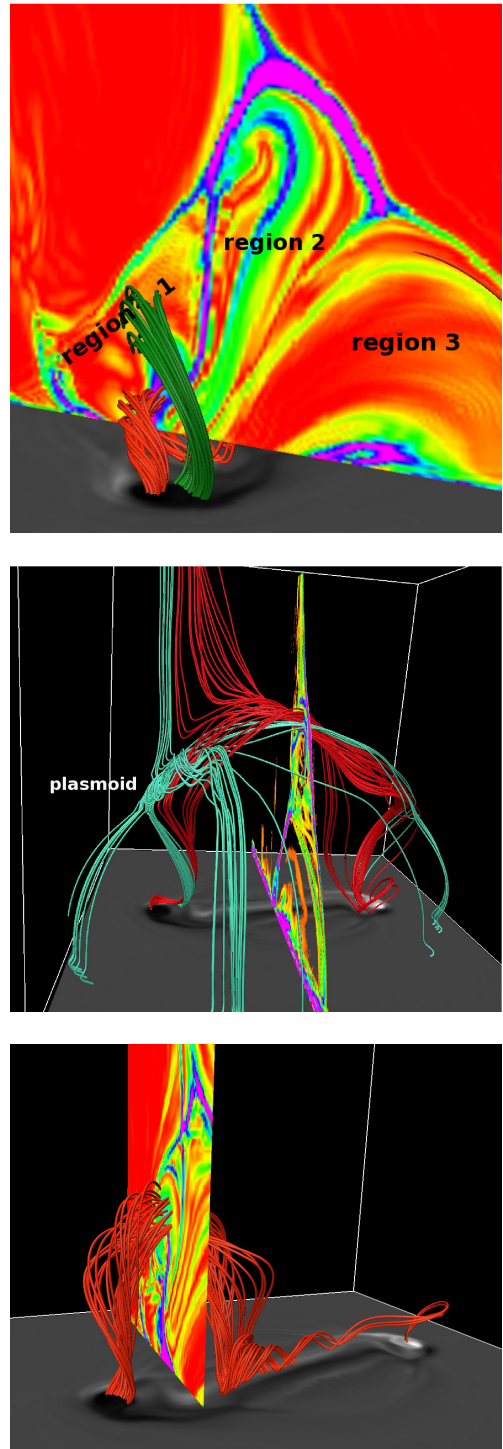


Figure 13. Top and center: Field line and electric current configuration at the start of the second eruption ($t = 66$ min). Top panel: map of $|j|/|B|$ at a vertical plane near the strong negative photospheric polarity ($y = 6.3$ Mm) including two flux ropes that erupt later on. Center: illustration of the field line topology associated with the prominent null point situated in the domain above the negative polarity. Bottom panel: rising twisted rope at $t = 69.5$ min, illustrating the evolution of eruption number two in the experiment. The $|j|/|B|$ vertical map shows an expanding and rotating bubble-like region which contains the erupting rope.

of the figure, drawn for $t = 69.5$ min. There, we see a roundish, bubble-shaped domain in the vertical plane pierced by a flux rope (drawn in red) that has a set of

footpoints rooted in the strong negative flux concentration while the other end delineates the PIL as it gets near the other polarity. The bubble is rising in that plane with velocities in excess of 100 km sec^{-1} . The plasma attached to the erupting rope has low temperatures, $1 - 4 \cdot 10^5 \text{ K}$, and relatively high densities compared with its surroundings, e.g., on the order of 10^{11} cm^{-3} (in either case about one order of magnitude off the values around the rope). The rope is moderately twisted (say, between 1 and 2 turns between the two footpoints), so the eruption may follow the development of a kink instability in it. In support of this hypothesis is the fact that the erupting rope appears to be converting part of its twist into writhe, in some ways resembling the evolution modeled by Török & Kliem (2005); also the PIL underneath the erupting rope gets increasingly hook-like. On the other hand, the initial shape of the rope (as in the left panel) is more like a semi-torus, so we cannot exclude that a torus instability (Kliem & Török 2006) is also helping propel the eruption. Finally, in the very early stages of this eruption there is a current concentration right below the rope that corresponds to an abrupt change of orientation of the field lines there. Hence, a certain amount of reconnection below the rope may partially be driving the eruption. The peak kinetic energy associated with this eruption is quite similar to the peak kinetic energy associated with the first one, namely of order $8 \cdot 10^{26} \text{ erg}$.

6.2.3. The third eruption

By time $t = 74 \text{ min}$, a third violent eruptive process takes place in the emerged domain, this time in the positive surface-polarity end of the active region, located in the $y < 0$ semi-space. This eruption bears a number of similarities with the second one, but is not fully equivalent to it since the field configuration of the whole emerged domain has no left-right symmetry with respect to the $y = 0$ vertical plane. The initial configuration of the field lines above the positive polarity is also of the twisted magnetic arch type with a PIL underneath with hook-like appearance (see the top panels of Figs. 11 and 12). Yet, the successive reconnection processes that have already occurred have led to a global connectivity pattern there which is quite different to the pattern above the negative polarity. For instance, there is no prominent null point above the positive polarity with fan-surface and spines extending for a long distance, as we saw for the negative polarity in Sec. 6.2.1. Also, like before, by drawing a map of $|\mathbf{j}|/|\mathbf{B}|$ on a vertical plane one can see a three-fold arrangement of connectivity regions, but, now, the unperturbed, twisted flux rope that winds its way above the PIL close to the strong photospheric polarity is found in the central region between the perturbed region and the hot loops and not on one side as was the case for the second eruption.

The external appearance of this eruption is not very different to the previous one: the unperturbed twisted flux rope around the strong photospheric polarity gets ejected upward, whereby it appears to convert part of its twist into writhe along the rise, as deduced both from the general shape of the rising arch as well as through the increasingly winding shape of the PIL at the photosphere. The erupting field lines have a sufficient number of turns around the rope axis to make it likely that the

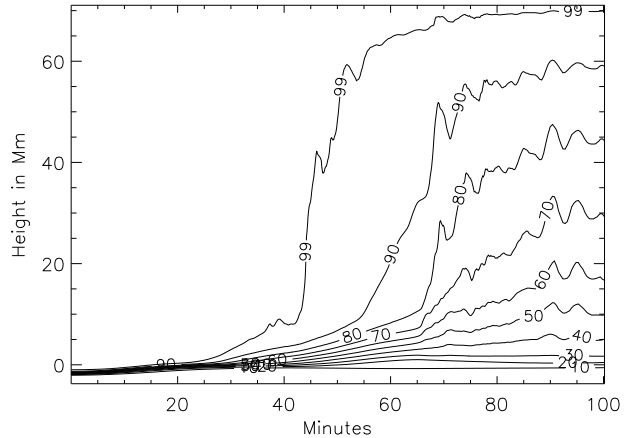


Figure 14. Redistribution of the B_y flux in time. Each curve corresponds to the height below which a given fraction of the total axial flux is contained (the fraction is annotated in each curve).

eruption is associated with the development of a kink instability. The strong perturbation rises and impacts on the ambient coronal field above the emerged domain. As for the two previous eruptions, the ambient open field is strong enough to withstand the impact: the perturbation is channeled along the inclined coronal field lines and creates a jet-shaped perturbation that reaches the top of the numerical domain. Concerning the kinetic energy associated with this eruption, there is no clean separation in the energy curve between eruption 2 and 3: during the latter, the kinetic energy in the volume goes to a maximum of about $1.1 \cdot 10^{27} \text{ erg}$.

7. TIME EVOLUTION OF GLOBAL QUANTITIES

7.1. Height distribution of the axial magnetic flux

At time $t = 0$ the ambient coronal field is contained in the xz vertical planes, so it is orthogonal to the axis of the embedded subphotospheric magnetic tube, which points in the y direction. This implies that any excess B_y -flux later found in the atmosphere has to result from the emergence of the initial flux tube. To investigate this process we calculate the flux across the central plane $y = 0$ between the bottom of the box and a given height:

$$\Phi_y(z, t) = \int_{z_{\text{bot}}}^z dz' \int_{-x_{\text{bound}}}^{x_{\text{bound}}} dx' B_y(x', y = 0, z', t), \quad (2)$$

with x_{bound} the value of $|x|$ at the position of the x -boundary. To make a simple representation, we normalize $\Phi_y(z, t)$ with the total flux across that plane (which is a constant), and represent the inverse function, i.e., the height at which a given fraction of the total flux is reached. Fig. 14 shows the inverse function for percentages in 10% steps: the curve labeled '90', for instance, shows the height below which 90% of the initial flux is contained; the one below corresponds to 80% and so on.

We see how the flux tube initially ($t \lesssim 25 \text{ min}$) rises very slowly towards the photosphere. Thereafter, it starts its expansion into the corona, first gradually and then at a faster speed. Yet, until $t \approx 65 \text{ min}$ only a small fraction of the axial flux reaches high into the corona. By that time the situation changes dramatically and axial

flux is expelled in a short burst into the coronal domain; this corresponds to the first eruptive event of Sec. 6. After that event, roughly 50% of the total axial flux is found above 10 Mm over the photosphere, which shows how effective the eruption is in pushing axial flux far up into the coronal region in comparison to the previous standard jet phase. In the later phases, the spreading of flux slows down and the curves show an oscillatory behavior, most likely caused by the non-equilibrium ensuing from the rapid ejection. Notice that in this plane ($y = 0$) the following eruptions do not leave any major imprint in terms of redistribution of axial flux, which is a further indication that they take place mostly in the flanks of the active region.

7.2. Connectivity between the submerged field and the atmosphere. The unsigned photospheric flux

The field lines of the initial submerged tube connect the two vertical $y = \text{const}$ planes at the boundary of the box with each other. As the tube surges into the atmosphere, part of those initial field lines reconnect with the ambient coronal field. We investigate the change in connectivity of the initial tube by tracing at different times a large number of magnetic field lines from a fixed circular area on one of the y -boundaries (hereafter called *the initial circle*): this circle covers the location of the initial submerged flux tube and a further area around it so that at later times it still covers most of the flux tube as it slowly diffuses out and sinks. The connectivity of the field lines starting from that circle can be divided into two groups: one (the *tube flux* for short) that connects the circle with a similar circle (but with 50% larger radius) at the opposite y -boundary (the *target circle*), and then the complementary set, consisting mostly of field lines that connect to the open field in the corona (here called *open flux*). Choosing a larger radius for the target circle helps prevent misidentifications of the connectivity class because of field line integration inaccuracies.

Fig. 15 helps quantify the connectivity changes along time. The full and dash-dotted lines give the fraction of the magnetic flux in the initial circle that belongs to the *tube*- and *open*-flux connectivity classes, respectively; the dash-dot-dot line gives their sum which is not constant in time since a small amount of flux diffuses or is advected out of the initial circle). We first see that at $t = 0$, most (90%) of the flux in the initial circle is part of the tube. The solid and dash-dotted curves are roughly horizontal until $t = 20$ minutes, with the flux thereafter changing connectivity class in a monotonic fashion until $t = 58$ minutes. This is followed by a much slower decline of the solid curve (with a mirrored pattern in the dash-dotted one) until $t = 63$ minutes, where a rapid and relatively small change occurs as a result of the first eruption. Toward the end of the experiment only a small amount of flux is still connecting the two ends of the flux tube. Seen from the surface, we expect the strong bipolar flux concentrations at the photosphere to lose their initial mutual connectivity and instead end up connecting almost entirely to the ambient flux in the corona.

The thick dashed curve in Fig. 15 provides related information: the curve shows the integrated unsigned magnetic flux through the photosphere with the flux of the initial coronal field subtracted, the whole being divided

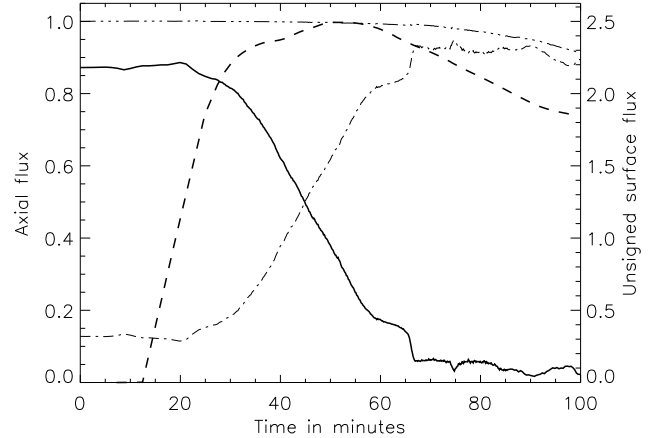


Figure 15. Change in time of the amount of flux connecting the two subphotospheric roots of the magnetic tube (left-hand ordinate axis). The curves represent the flux connecting the roots (solid), the open flux (i.e., the flux with other connectivities, dash-dotted) and their sum (dash-dot-dot), all normalized to the initial value of the sum. The thick dashed curve shows the unsigned vertical magnetic flux of either polarity through the photosphere, normalized to the initial axial flux in the tube (right-hand ordinate axis).

by two:

$$\frac{1}{2} \left(\int_{z=0} |B_z(x, y, t)| dx dy - \int_{z=0} |B_z(x, y, t=0)| dx dy \right). \quad (3)$$

Given that most of the emerged flux at the photosphere is in the strong-field concentrations, where $|B_z| \gg |B_z(t=0)|$, that quantity approximates well the total emerged flux of either polarity at the surface. The thick dashed-line of Fig. 15 shows Eq. 3 in units of the axial flux of the initial tube. The curve shows the arrival of flux at the surface ($t \approx 10$ min) and the rapid subsequent rise to a value well above the initial axial flux due to the contribution of the azimuthal components of the field in the rising twisted tube. There is a good correspondence in time between the top region of the dashed line and the phase of rapid change of connectivity shown by the full and dash-dotted lines. Finally, from $t \approx 55$ onward, the total unsigned surface flux decays slowly, and the eruptions and late episodes in the corona have no counterpart in it: this is expected since the changes in the coronal field are in no position to modify the flux in the photosphere.

As a final remark, note that, given the complication of the topological changes for the field in the box, Fig. 15 cannot be used to derive a global rate of reconnection between the emerging tube and the coronal field, but, at best, a lower limit for it (see the related discussion by Parnell et al. 2008).

8. DISCUSSION

8.1. Comparison with jet observations: standard jets and blowout jets

There are various remarkable qualitative and quantitative similarities between our results and those of a number of recent observational papers. We start by considering the values of the plasma temperature and density for the jets mentioned in the introduction. The range of temperatures obtained by Shimojo & Shibata (2000) fit

well with the temperatures obtained by us for a generic height in the jet (Fig. 6), while the values of Madjarska et al. (2012) are rather on the low side compared with ours. During its hottest phase, the jet in the experiment also has low densities, as explained in Sec. 4.1. At that time we measure densities between about 10^9 cm^{-3} and a few times that value depending on the position along the jet, which match well the values quoted by those authors. In any case, note that Figs. 6 and 8 contain peak values of T and v , and that (see Fig. 5) the very fast jet strands may be small in terms of the resolution element of the satellite instruments: a good comparison with observations requires a much deeper study than is possible within this paper.

In the introduction we also mentioned the statistical study of Hinode X-ray polar jets by Savcheva et al. (2007). The velocities they obtain, distributed between 70 and about 500 km sec^{-1} and peaking at 160 km sec^{-1} fit well with our simulations (Figures 6 and 8), in which we obtain values from 100 to 300 km sec^{-1} (400 km sec^{-1} in the current sheet) along the main phase of the jet. Concerning the observed longitudinal sizes (between 10 and 120 Mm), we note that the jet in the numerical experiment easily reaches the top boundary placed at a height of 70 Mm, so the expectation is that the jet motion will continue to substantially larger heights. The peak height in the observation may be indirectly limited by the weakness of the signal as the plasma expands with height. For the width of the jet, Savcheva et al. (2007) mention some 8 Mm; for the comparison, we use our Fig. 5, from which we deduce a transverse size of about 10 Mm. The lifetime of the jets was between 5 and 30 min in the study of Savcheva et al., peaking at 10 min. Referring to our Fig. 6, we see our jet to last some 30 min, i.e., toward the upper bound of the observations. However, it is unclear for which fraction of that time the jet would have sufficient emission in the X-Ray range to be detectable by the XRT instrument. Finally, the jet is seen to have a drift velocity in the horizontal direction as a consequence of the reconnection process (Sec. 4.2). From the observations the drift velocity is found to be on the order of $0 - 35 \text{ km sec}^{-1}$. In our experiment we have some 8 km sec^{-1} for the drift velocity at maximum (end of Sec. 4.2). All in all, the comparison between theory and the statistics of the observations is satisfactory: the present experiment provides values for the different magnitudes (well) within the ranges observed for actual X-ray jets in the Sun.

Of particular interest is the comparison with the recent observational results concerning the so-called *blowout jets*. Using Hinode/XRT and Stereo/EUVI observations, Moore et al. (2010) deduced a dichotomy of coronal jet evolutionary patterns. Those authors detected that an important fraction of the jet events, around one third of them, presents an eruptive pattern accompanying the jet ejection itself. For this class of jets they find anomalous X-ray brightenings below the jet additionally to the major bright points of standard jets, followed by the eruption of material with temperatures one or two orders of magnitude below coronal values. Further observations of jets with associated energy release bursts are those of Madjarska (2011) and Liu et al. (2011). In the first of those, in particular, the author presented observations of

a jet with four successive short-duration energy release bursts over a time period of 20 minutes.

The numerical experiment we are presenting in this paper yields in a natural fashion a collection of eruptive phenomena directly associated with the magnetic configuration around a jet following flux emergence which may be the counterpart to these observational facts. We have found ejections of, basically, two different kinds that we tentatively ascribe to (a) a tether-cutting reconnection pattern occurring in the coronal remnant of an emerged magnetic region and taking place in the complicated topology left over by the reconnection that led to the jet in the first place; and (b) a secondary twisted flux rope ejection pattern that may be caused by the development of a kink instability (or perhaps of a torus instability). For the identification with observed features it may be of interest to note that the eruptions in the experiment first go through a direct impulsive phase with high velocities oriented in the outward direction, later yielding a more chaotic velocity pattern when the eruption impinges on the surrounding plasma, especially on the ambient coronal field, which in our experiment is strong enough to divert the outgoing flow. Analyzing the second eruption in our experiment (Sec. 6.2.2), we have seen that the ejected flux rope contains cool ($1 - 4 \cdot 10^5 \text{ K}$) and dense (almost 10^{11} cm^{-3}) material during the initial impulsive phase, values which differ by about one order of magnitude from those of the surroundings. A detailed analysis of further aspects of this multi-faceted phenomenon is necessary to ascertain its possible identification with the results of Moore et al. (2010).

8.2. *The eruptions and their relation to previous experiments*

In the numerical simulation literature there are different reports of eruptions resulting directly or indirectly from an episode of flux emergence into the atmosphere (e.g., Fan & Gibson 2003, 2004; Manchester et al. 2004; Archontis & Török 2008; Archontis & Hood 2008, 2012; MacTaggart & Hood 2009; Török et al. 2009), or, also, from processes related with the development of a kink- or torus instability in a magnetic configuration (Török & Kliem 2003, 2005; Pariat et al. 2009, 2010; Aulanier et al. 2010). Manchester et al. (2004) followed the emergence of a flux tube into a nonmagnetic coronal domain. They explain how after an initial phase of emergence from the interior, Lorentz-force driven motions lead to the conversion of the emerged magnetic domain into a sheared arcade; its upper part starts to separate from the lower part, which is loaded with mass and must stay behind. The process results in local stretching of the field lines in the vertical direction just above the photosphere and formation of a vertical current sheet above the polarity inversion line. As the current builds up in strength, a fast reconnection process is initiated in the arcade. This rapidly creates a new flux rope above the current sheet that moves upwards with a speed much higher than the rise speeds in the previous phases and constitutes an eruption. Archontis & Hood (2012) expanded this work by conducting experiments with different ambient coronal field configurations. They found the same eruptive behavior of the emerging flux tube independently of the coronal field; they also showed that the dynamics follow-

ing the eruption depends on both the twist of the initial tube and the orientation of the imposed coronal field. Depending on the parameter combination, the erupting flux tube will either escape up through the atmosphere or be confined by the overlying coronal magnetic flux.

The eruptions discussed in those investigations are comparable to our first eruption. However, given the previous evolution of the system in our case, with four connectivity patterns resulting from the emergence of the initial submerged rope into a slanted coronal field (Fig. 4), we had to ascertain the complicated changes of connectivity of different regions caused by the eruption (Sec. 6.1) and, also, determine regions in the emerged volume which remain unaffected by it and, in fact, turn out to be ejected themselves later on (as in eruptions 2 and 3). We conclude that the standard sheared arcade model requires to be modified to deal with the more complex field line situation found in our experiment. The additional complexity also allows information from the reconnection process to spread over a larger volume and therefore indirectly stress neighboring flux regions that would not be reached in the classical picture.

In a different approach to simulate jet formation Pariat et al. (2009, 2010) conducted a series of experiments in which a vertical dipole is embedded in a background monopolar field. This gives a magnetic topology in which a 3D null point hovers above the parasitic polarity region with a near vertical spine axis that in one direction reaches the model photosphere close to the center of the parasitic polarity and in the other follows the open field upwards. Stress is imposed in the form of a systematic rotation of the parasitic polarity region. The twisting of the spine axis eventually destroys the symmetries in the system and drives a kink instability. The evolution of the null point is, in a way, comparable to what we found for the null point near the site of the second eruption – disrupting the fan plane by building up a current sheet that splits the external part of the spines’ axis as also seen in dedicated null point investigations (see Galsgaard & Pontin 2011 and references therein; see also Török et al. 2009; Masson et al. 2009 for other experiments with driven fan-spine reconnection events.) However, from Sec. 6.2, it is clear that it is not a kink instability associated with the rotation of the spine axis that is responsible for the second and third eruptions. Instead we think that in our case it is a twisted rope with the shape of a highly inclined Ω loop at the end points of the PIL that becomes unstable and erupts, thereby converting twist into writhe. So we assume that the driver for the eruption is more of the kink- or torus-instability kind of a semitoroidal twisted rope, perhaps a combination of the two.

8.3. Flux emergence, $H\alpha$ surges and CaII jets

In this experiment we have found that a substantial amount of cool and dense material accumulates around the main dome of emerged magnetic right before and during the main phase of jet ejection; the accumulated material has densities at a given height typically one to two orders of magnitude above those at that height in the unperturbed initial corona (Sec. 5, Fig. 9). The maximum accumulation occurs in the domain below the jet, where it can reach a vertical extent of several Mm. Through extended Lagrange tracing we have determined that a

relevant part of the plasma in that cool and dense wall originally was in the emerged magnetic dome and has been bodily transferred to the wall accompanying field lines that change connectivity at some height, but the plasma element itself need not have gone through the reconnection site. Other plasma elements in the wall were originally located at comparatively low levels in the ambient corona when the flux tube arrived, from where they were transported to the wall, again in many cases accompanying field lines reconnecting somewhere along their length. The velocities measured in the dense domain are not large, typically less than 50 km sec^{-1} , and the temperatures range between a few times 10^4 K and a few times 10^5 K , i.e., mostly transition-region values. These cool features do not have any obvious jet appearance; in particular, from the morphology of the distributions of velocity, temperature or density, one cannot say that they contain, or consist of, collimated motions. It is also unclear what the fate of this cool region would be if heat conduction had been included in the experiment.

Now, a substantial amount of observational and theoretical literature has been devoted to the quasi-simultaneous appearance of hot X-ray/EUV jets and cold $H\alpha$ surges or CaII-H jets (see, e.g., Schmieder et al. 1995; Canfield et al. 1996; Chae et al. 1999; Alexander & Fletcher 1999; Jiang et al. 2007). A theoretical interpretation has been based on the possible simultaneous presence of cold and hot jets in two-dimensional numerical experiments of flux emergence into magnetized coronae (Yokoyama & Shibata 1996; Nishizuka et al. 2008; see also Takasao et al. 2013). Yokoyama & Shibata (1996) state that the cool plasma is chromospheric in origin and is, using the words in that paper and in Nishizuka et al. (2008), *ejected or accelerated by the sling-shot effect due to reconnection, which produces a whip-like motion*. The relation of this description for the 2D experiments with the 3D processes analyzed in our Sec. 5 needs further exploration. Nishizuka et al. (2008) also suggest that the cool jet may result from the asymmetry of the plasma properties on either side of the main current sheet separating the ambient corona (hot and thin plasma) from the emerged domain (cool and dense): this would lead to the formation of both a fast hot jet and a cool, slower jet. In any case, in view of the available theoretical and observational results, we think that a clear identification of the cool structures in 2D or 3D with observed cool jets does certainly require a more in-depth comparison between simulations and observations.

8.4. Summary

We have studied the fast and hot jet and the violent eruptions that follow the emergence of organized magnetic flux from the solar interior into a corona with a uniform, inclined magnetic field. Here is a summary of some major results:

- The quantitative and qualitative aspects of the 3D structure and evolution of the *standard jet* that is launched following the collision of emerging and ambient field systems have been explained (Sec. 4)
- In the standard jet phase, the reconnection process that takes place at the interface between the colliding flux systems has been seen to be topologically complex, including both magnetic null points

and plasmoids. This results in the formation of complicated connectivity patterns, and spatial and temporal variation of physical variables (Sec. 4.3).

- An indirect product of the reconnection process in the standard jet phase is the formation of a dense and cool 3D plasma structure surrounding the emerged plasma region (Sec. 5).
- The different physical parameters of the standard jet resulting from our experiment are well within the observational ranges obtained in the statistical study of Savcheva et al. (2007).
- After the standard jet phase, a number of violent eruptions of the magnetic field structure take place in different volumes of the emerged plasma dome. They show a variety of origins and patterns of evolution. This covers the traditional sheared arcade instability as described by Manchester et al. (2004), but also other types that are probably related to the development of a kink or torus instability.
- The global scheme resulting from this experiment (flux emergence, standard jet launching and violent eruptions of different physical origins) may provide an explanation for the phenomenon of blowout jets described by Moore et al. (2010).

Financial support by the Spanish Ministry of Research and Innovation through projects AYA2007-66502, AYA2011-24808 and CSD2007-00050 and by the European Commission through the SOLAIRE Network (MTRN-CT-2006-035484) is gratefully acknowledged. We are grateful to ISSI (Berne, Switzerland) for hosting two series of workshops (on magnetic flux emergence and on coronal jets) where parts of this work were presented. The results in this paper have been achieved through generous computing time grants by the European Consortia PRACE (JUGENE and JURIPA, Jülich) and DEISA (HLRS, Stuttgart), as well as by BSC (MareNostrum, National Supercomputing Center, Barcelona), GCS/NIC (Danish Center for Scientific Computing, Copenhagen), and IAC (LaPalma supercomputer, Canary Islands): their permission to use the resources and their support are greatly appreciated. 3D visualisation has been carried out using the VAPOR package (UCAR, www.vapor.ucar.edu). The useful comments by an anonymous referee are gratefully acknowledged. We are also grateful for many conversations with M. Madjarska on the observations and the physics of coronal jets as well as for comments on the manuscript by I. Ugarte Urra.

REFERENCES

- Alexander, D., & Fletcher, L. 1999, *Sol. Phys.*, 190, 167
 Archontis, V., Galsgaard, K., Moreno-Insertis, F., & Hood, A. W. 2006, *ApJ*, 645, L161
 Archontis, V., & Hood, A. W. 2008, *ApJ*, 674, L113
 —. 2012, *A&A*, 537, A62
 Archontis, V., Moreno-Insertis, F., Galsgaard, K., Hood, A., & O’Shea, E. 2004, *A&A*, 426, 1047
 Archontis, V., Moreno-Insertis, F., Galsgaard, K., & Hood, A. W. 2005, *ApJ*, 635, 1299
 Archontis, V., & Török, T. 2008, *A&A*, 492, L35
 Aulanier, G., Török, T., Démoulin, P., & DeLuca, E. E. 2010, *ApJ*, 708, 314
 Canfield, R. C., Reardon, K. P., Leka, K. D., Shibata, K., Yokoyama, T., & Shimojo, M. 1996, *ApJ*, 464, 1016
 Carmichael, H. 1964, *NASA Special Publication*, 50, 451
 Chae, J., Qiu, J., Wang, H., & Goode, P. R. 1999, *ApJ*, 513, L75
 Cirtain, J. W., et al. 2007, *Science*, 318, 1580
 Culhane, J. L., et al. 2007a, *Sol. Phys.*, 243, 19
 Culhane, L., et al. 2007b, *PASJ*, 59, 751
 Ding, J. Y., Madjarska, M. S., Doyle, J. G., & Lu, Q. M. 2010, *A&A*, 510, A111
 Ding, J. Y., Madjarska, M. S., Doyle, J. G., Lu, Q. M., Vanninathan, K., & Huang, Z. 2011, *A&A*, 535, A95
 Doschek, G. A., Landi, E., Warren, H. P., & Harra, L. K. 2010, *ApJ*, 710, 1806
 Fan, Y. 2001, *ApJ*, 554, L111
 Fan, Y., & Gibson, S. E. 2003, *ApJ*, 589, L105
 —. 2004, *ApJ*, 609, 1123
 Forbes, T. G., & Priest, E. R. 1984, *Sol. Phys.*, 94, 315
 Galsgaard, K., Archontis, V., Moreno-Insertis, F., & Hood, A. W. 2007, *ApJ*, 666, 516
 Galsgaard, K., & Pontin, D. I. 2011, *A&A*, 534, A2
 Harvey, K. L., & Recely, F. 2002, *Sol. Phys.*, 211, 31
 Haynes, A. L., & Parnell, C. E. 2007, *Physics of Plasmas*, 14, 082107
 Heyvaerts, J., Priest, E. R., & Rust, D. M. 1977, *ApJ*, 216, 123
 Hirayama, T. 1974, *Sol. Phys.*, 34, 323
 Innes, D. E., McIntosh, S. W., & Pietarila, A. 2010, *A&A*, 517, L7
 Jiang, Y. C., Chen, H. D., Li, K. J., Shen, Y. D., & Yang, L. H. 2007, *A&A*, 469, 331
 Kano, R., et al. 2008, *Sol. Phys.*, 249, 263
 Kliem, B., & Török, T. 2006, *Physical Review Letters*, 96, 255002
 Kopp, R. A., & Pneuman, G. W. 1976, *Sol. Phys.*, 50, 85
 Liu, C., Deng, N., Liu, R., Ugarte-Urra, I., Wang, S., & Wang, H. 2011, *ApJ*, 735, L18
 MacTaggart, D., & Hood, A. W. 2009, *A&A*, 508, 445
 Madjarska, M. S. 2011, *A&A*, 526, A19
 Madjarska, M. S., Huang, Z., Doyle, J. G., & Subramanian, S. 2012, *A&A*, 545, A67
 Madjarska, M. S., & Wiegmann, T. 2009, *A&A*, 503, 991
 Magara, T. 2001, *ApJ*, 549, 608
 Manchester, IV, W., Gombosi, T., DeZeeuw, D., & Fan, Y. 2004, *ApJ*, 610, 588
 Masson, S., Pariat, E., Aulanier, G., & Schrijver, C. J. 2009, *ApJ*, 700, 559
 McLaughlin, J. A., Verth, G., Fedun, V., & Erdélyi, R. 2012, *ApJ*, 749, 30
 Mikic, Z., Barnes, D. C., & Schnack, D. D. 1988, *ApJ*, 328, 830
 Miyagoshi, T., & Yokoyama, T. 2003, *ApJ*, 593, L133
 Moore, R. L., Cirtain, J. W., Sterling, A. C., & Falconer, D. A. 2010, *ApJ*, 720, 757
 Moore, R. L., & Roumeliotis, G. 1992, in *Lecture Notes in Physics*, Berlin Springer Verlag, Vol. 399, IAU Colloq. 133: Eruptive Solar Flares, ed. Z. Svestka, B. V. Jackson, & M. E. Machado, 69
 Moreno-Insertis, F. 2006, in *Astronomical Society of the Pacific Conference Series*, Vol. 369, *New Solar Physics with Solar-B Mission*, ed. K. Shibata, S. Nagata, & T. Sakurai, 335+
 Moreno-Insertis, F., Galsgaard, K., & Ugarte-Urra, I. 2008, *ApJ*, 673, L211
 Murray, M. J., Hood, A. W., Moreno-Insertis, F., Galsgaard, K., & Archontis, V. 2006, *A&A*, 460, 909
 Murray, M. J., van Driel-Gesztelyi, L., & Baker, D. 2009, *A&A*, 494, 329
 Nishizuka, N., Shimizu, M., Nakamura, T., Otsuji, K., Okamoto, T. J., Katsukawa, Y., & Shibata, K. 2008, *ApJ*, 683, L83
 Nisticò, G., Bothmer, V., Patsourakos, S., & Zimbardo, G. 2009, *Sol. Phys.*, 259, 87
 Nordlund, A., & Galsgaard, K. 1997, *A 3D MHD code for Parallel Computers*, Tech. rep., Niels Bohr Institute
 Pariat, E., Antiochos, S. K., & DeVore, C. R. 2009, *ApJ*, 691, 61
 —. 2010, *ApJ*, 714, 1762
 Parnell, C. E., Haynes, A. L., & Galsgaard, K. 2008, *ApJ*, 675, 1656
 Patsourakos, S., Pariat, E., Vourlidis, A., Antiochos, S. K., & Wuelser, J. P. 2008, *ApJ*, 680, L73

- Pontin, D. I., Bhattacharjee, A., & Galsgaard, K. 2007, *Physics of Plasmas*, 14, 052109
- Priest, E. R., & Pontin, D. I. 2009, *Physics of Plasmas*, 16, 122101
- Savcheva, A., et al. 2007, *PASJ*, 59, 771
- Schmieder, B., Shibata, K., van Driel-Gesztelyi, L., & Freeland, S. 1995, *Sol. Phys.*, 156, 245
- Shibata, K., Tajima, T., Matsumoto, R., Horiuchi, T., Hanawa, T., Rosner, R., & Uchida, Y. 1989, *ApJ*, 338, 471
- Shibata, K., et al. 1992, *PASJ*, 44, L173
- Shimojo, M., Hashimoto, S., Shibata, K., Hirayama, T., Hudson, H. S., & Acton, L. W. 1996, *PASJ*, 48, 123
- Shimojo, M., & Shibata, K. 2000, *ApJ*, 542, 1100
- Sturrock, P. A. 1966, *Nature*, 211, 695
- . 1989, *Sol. Phys.*, 121, 387
- Subramanian, S., Madjarska, M. S., & Doyle, J. G. 2010, *A&A*, 516, A50
- Takasao, S., Isobe, H., & Shibata, K. 2013, *ArXiv e-prints*
- Török, T., Aulanier, G., Schmieder, B., Reeves, K. K., & Golub, L. 2009, *ApJ*, 704, 485
- Török, T., & Kliem, B. 2003, *A&A*, 406, 1043
- . 2005, *ApJ*, 630, L97
- Wang, Y.-M., et al. 1998, *ApJ*, 508, 899
- Wilhelm, K. 2006, *A&A*, 455, 697
- Yokoyama, T., & Shibata, K. 1995, *Nature*, 375, 42
- . 1996, *PASJ*, 48, 353